A B-spline based gradient-enhanced micropolar implicit material point method for large localized inelastic deformations

M. Neuner[a,*], A. Dummer[a], S. Abrari Vajari[b], P. Gamnitzer[a], H. Gimperlein[a], C. Linder[b], G. Hofstetter[a]

[a] *Institute of Basic Sciences in Engineering Sciences, University of Innsbruck, Austria*
[b] *Department of Civil and Environmental Engineering, Stanford University, Stanford, CA, USA*

Abstract

The quasi-brittle response of cohesive-frictional materials in numerical simulations is commonly represented by softening plasticity or continuum damage models, either individually or in combination. However, classical models, particularly when coupled with non-associated plasticity, often suffer from ill-posedness and a lack of objectivity in numerical simulations. Moreover, the performance of the finite element method significantly degrades in simulations involving finite strains when mesh distortion reaches excessive levels. This represents a challenge for modeling cohesive-frictional materials, given their tendency to experience strongly localized deformations, such as those occurring during shear band dominated failure. Hence, accurate modeling of the response of cohesive-frictional solids is a demanding task. To address these challenges, we present an extension of the material point method (MPM) for the unified gradient-enhanced micropolar continuum, aiming at the analysis of finite localized inelastic deformations in cohesive-frictional materials. The generalized gradient-enhanced micropolar continuum formulation is employed to tackle challenges related to localization and softening material behavior, while the MPM addresses issues arising from excessive deformations. The method leverages a B-spline formulation for the rigid background mesh to mitigate the well-known cell crossing errors of the MPM as well as locking behavior in case of inelastic deformations. To demonstrate the performance of the method, 2D and 3D numerical studies on localized failure in sandstone in plane strain compression and triaxial extension tests are presented. A comparison with finite element results confirms the suitability of the formulation. Moreover, an efficient numerical implementation of the formulation is presented, and it is demonstrated that the additional MPM specific overhead is negligible.

Keywords: Material point method, Micropolar continuum, Gradient-enhanced continuum, B-spline, Shear failure

1. Introduction

Cohesive-frictional materials, also known as geomaterials or quasi-brittle materials [4], describe a large class of solids whose constitutive behavior is dominated by friction and cohesion between individual particles or grains. These materials arise in almost all engineering disciplines with examples such as concrete, mortar, rock, rock mass, clay, bone, fibre reinforced composites, tough ceramics, soils, and cemented sands. Such materials, even at low stress levels, exhibit nonlinear elastic and inelastic behavior. Other characteristics include a low resistance in tension and a potentially high compressive strength, a pronounced pressure dependency of strength, and complex failure mechanisms depending on the stress state.

*Corresponding author

Email addresses: matthias.neuner@uibk.ac.at (M. Neuner), alexander.dummer@uibk.ac.at (A. Dummer), abrari@stanford.edu (S. Abrari Vajari), peter.gamnitzer@uibk.ac.at (P. Gamnitzer), heiko.gimperlein@uibk.ac.at (H. Gimperlein), linder@stanford.edu (C. Linder), guenter.hofstetter@uibk.ac.at (G. Hofstetter)

The mechanical response of cohesive-frictional materials is greatly influenced by the microstructure of the solid as well as the deformations at the microscale. For instance, cohesive-frictional materials with distinct cohesive particle bonds might exhibit a fracturing and cracking material response in tension or unconfined compression. This behavior is caused by discrete crack formation characterized by a fracture process zone of finite size ahead of the crack tip. In this fracture process zone, microcracks emerge and coalesce to form distinct stress free macroscropic cracks – a process known as quasi-brittle cracking [5]. Due to the presence of a fracture process zone with finite size, quasi-brittle cracking is characterized by an inherent material length associated with the microstructure of the solid. Additionally, in confined compression and shear, strongly localized zones of large inelastic deformations emerge, frequently in the form of shear bands, kink bands, or fault zones. Similar to quasi-brittle fracture process zones, these localized regions of inelastic deformations are dominated by an apparent size effect, which is, for example, evidenced by the finite width of shear bands. The characteristic dimensions of such localized zones are related to deformations at the microstructure of a material, to the scale of the microstructure, and to material heterogeneities.

1.1. Constitutive modeling of cohesive-frictional materials

In classical pure continuum models, the quasi-brittle response of cohesive-frictional solids is often captured by means of softening plasticity or continuum damage mechanics, or a combination thereof. However, classical models, which do not represent any intrinsic characteristic material length scale, suffer from ill-posedness and a lack of objectivity, i.e., a pronounced mesh sensitivity in numerical simulations [43]. Additionally, in material models for cohesive-frictional materials based on the theory of plasticity, non-associated plastic flow rules are commonly employed for representing the volumetric inelastic behavior in a realistic manner. However, non-associated plastic flow can lead to unstable material behavior, which manifests itself in the form of localized deformations, structural softening behavior, and accordingly, a pathological mesh sensitivity of the results in numerical simulations [18, 7].

To resolve these issues in the context of pure continuum models, various different approaches have been proposed and investigated, for instance, so-called strongly nonlocal and weakly nonlocal [69] generalized continuum models, which emerged in the past century. Such approaches are based on the assumption that the response of a material particle is not only influenced by its own loading history but also by the state within a certain finite or potentially infinite neighborhood. See [50] for a historical overview.

From a numerical point of view, weakly and strongly nonlocal generalized continuum models formulated implicitly by means of coupled systems of partial differential equations are amenable to efficient and robust numerical implementations, as they readily fit the concepts of many established and well understood numerical methods, such as the Finite Element Method (FEM). Particular examples of such generalized continuum theories are: (i) the micromorphic continuum [29, 26], taking into account the deformation of the microstructure by means of an independent microdeformation field, (ii) the microstretch and micropolar (or Cosserat [15]) continua [27], which are both special cases of Eringen's micromorphic continuum assuming certain kinematic restrictions for the microdeformation, (iii) strain gradient formulations [79, 51, 1, 8], and (iv) implicit gradient-enhanced continuum formulations with gradients of internal state variables [64]. Interested readers are referred to [33, 34, 32] for a systematic thermodynamic approach to such formulations.

One key aspect of generalized continuum formulations is that they may serve as a remedy for the well-known problems of classical continua with regard to localizing and softening material behavior. Moreover, the formulation of generalized continuum models for material failure can be physically motivated by the micromechanical behavior [65, 3, 24] of cohesive-frictional materials considering quasi-brittle fracture a nonlocal process.

For instance, gradient-enhanced models with gradients of internal state variables, taking into account the nonlocal influence of spatially interacting microcracks, are particularly well suited for representing quasi-brittle cracking in tension. However, such formulations are potentially not sufficient for modeling the complex kinematics of shear band dominated failure. On the other hand, while micropolar continuum models in general provide no regularizing effect for quasi-brittle cracking in tension [42], they represent a proper framework for modeling shear band dominated failure and for regularizing non-associated plasticity [58]. Hence, for a general continuum model representing the response of cohesive-frictional materials under a broad range of loading conditions ranging from cracking in tension to shear band dominated failure, both the size effect related to microstructural deformations and the nonlocal character of quasi-brittle failure in terms of interacting microcracks have to be taken into account.

Accordingly, Neuner et al. [58] proposed a gradient-enhanced micropolar approach for quasi-brittle failure of cohesive-frictional materials formulated in the small strain regime. Using the micropolar theory, the framework presented a proper remedy for the non-associated plastic flow issues, while the gradient-enhanced part accounted for the damage evolution. The novel framework was also validated based on several challenging experimental tests on concrete, including a comprehensive numerical study on a transverse shear test on concrete slabs reported in [59]. Motivated by these promising results, Neuner et al. [60] recently presented a thermodynamically consistent extension of the gradient-enhanced micropolar continuum to the finite strain regime, based on the concept of hyperelasto-plasticity. Continuing those efforts, Neuner et al. [57] formulated a damage-plasticity model for Red Wildmoor sandstone, investigating complex borehole breakout modes in soft rock. These works confirmed the potential of a unified gradient-enhanced micropolar formulation for investigating localized material failure in cohesive-frictional materials involving microdeformations.

1.2. Material point method for large inelastic deformations

It is well known that the performance of the classical Lagrangian FEM deteriorates substantially in simulations considering finite strains if mesh distortion becomes excessive. This may occur in particular for modeling shear band dominated failure of cohesive-frictional materials with strongly localized deformations, see Fig. 1. Accordingly, there is a strong demand for tailored numerical methods to overcome these limitations of the classical FEM. In the past decades, several alternative numerical methods have been developed for solving problems involving large displacements. Examples include the Particle Finite Element Method (PFEM) [62, 41], the Discrete Element Method (DEM) [16, 17], Smoothed Particle Hydrodynamics (SPH) [35, 31, 30, 20, 21, 87], meshfree methods such as the Reproducing Kernel Particle Method (RKPM) [48, 12, 11, 37, 6], or the Material Point Method (MPM) [77, 78].

A particularly promising method is the MPM, a Lagrangian particle method using a rigid background mesh for computing spatial derivatives and for assembling the global system of equations. Compared to, e.g., the DEM, the MPM is rooted in continuum mechanics, and for this reason, classical continuum models, e.g., developed in the context of the FEM, can be adopted easily. The MPM was developed initially by Sulsky et al. [77, 78], see also [19, 72] for recent overviews. The fundamental ideas of the MPM are the spatial discretization of a domain of interest by a finite number of material points (sometimes also denoted as particles), the use of an independent background mesh, i.e., fixed in space, for assembling and solving a global system of differential equations, and the use of suitable interpolation methods for passing information between material points and the background mesh, see Fig. 2 for an illustration of the original method.

In the MPM the history and thermodynamic state of the material are convecting with the material points, and accordingly, the method is commonly denoted a Lagrangian particle method, despite involving a background mesh. Although initially proposed for explicit time integration schemes, in the past years, implicit formulations of the MPM (iMPM) have also been presented [52, 36, 10, 83, 39, 40, 14, 66, 67]. Unconditionally stable implicit schemes can guarantee numerically stable solutions independently of the choice of time steps in transient simulations. Thus, especially if combined with techniques for error control, they are particularly well suited for

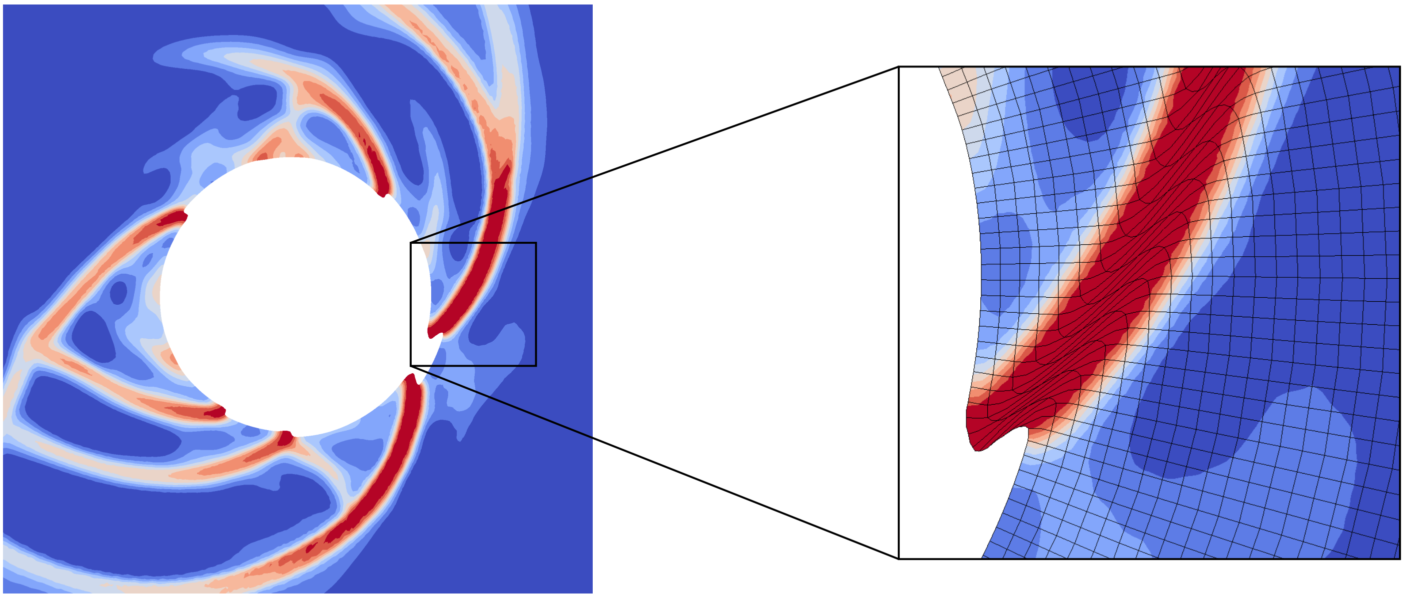

Figure 1: Contour plot of damage from a simulation of borehole breakout, using a finite strain gradient-enhanced micropolar damage-plasticity model for sandstone within the classical finite element method [57]. Large, localized deformations may deteriorate the performance of the classical finite element method due to excessive mesh distortion.

static and quasi-static analyses. Several applications reported in the literature demonstrate the great potential of the MPM, for instance for geomechanical problems [73, 80, 82], fracture modeling [44, 47, 53], or manufacturing processes of ultra-high temperature ceramics [66, 67].

Within the MPM, a major research effort is devoted to the development of improved interpolation procedures for passing information from the material points to the background mesh and vice versa. While the original MPM [77] did not consider a finite size of the material points and treated them as point masses, extensions such as the Generalized Interpolation MPM (GIMP) [2] with different variants uGIMP and cpGIMP [81], the Convected Particle Domain Interpolation techniques and extensions (CPDI, CPDI2) [71, 70], and the Dual Domain technique MPM (DDMP) [86] improve the MPM by assigning the material points a finite size and distinct shape, as well as accounting for the change in volume and shape of a material point undergoing deformations. This is achieved by assuming characteristic domain functions for each material point, which, together with the classical grid shape functions, are used in a convolution operation to obtain modified weight functions for the interpolation procedure. Thereby, an increased robustness and accuracy of the method is obtained, and numerical issues, such as cell boundary crossing errors or numerical fracture, can be remedied [72]. Another recent concept, the Partitioned Quadrature Material Point Method (PQMPM), modifies the numerical quadrature by considering material points consisting of subdomains during cell crossing [84].

Alternative approaches make use of higher order B-splines [74, 75], similar to Isogeometric FEM approaches [38], exploiting their higher order continuity to mitigate cell crossing errors, and for improved convergence properties. Additionally, the ease of the implementation of B-splines and the fact that they are less prone to locking compared to linear shape functions traditionally used in MPM are promising characteristics.

There are only a few reported applications of the MPM to generalized continua, such as the micropolar continuum, e.g., the explicit formulation by Ma and Sun [49]. Compared to explicit formulations, implicit formulations of the MPM are a considerably newer development, and accordingly, their formulation for generalized continuum models has not yet been investigated in detail. An extension of the iMPM to the purely elastic micropolar continuum was recently presented in [61], neglecting, however, inelastic material behavior and material failure. More specifically, micropolar continua are characterized by finite macroscopic deformations, including stretch, shear, and rotational components, alongside independent finite microrotations. These deformations

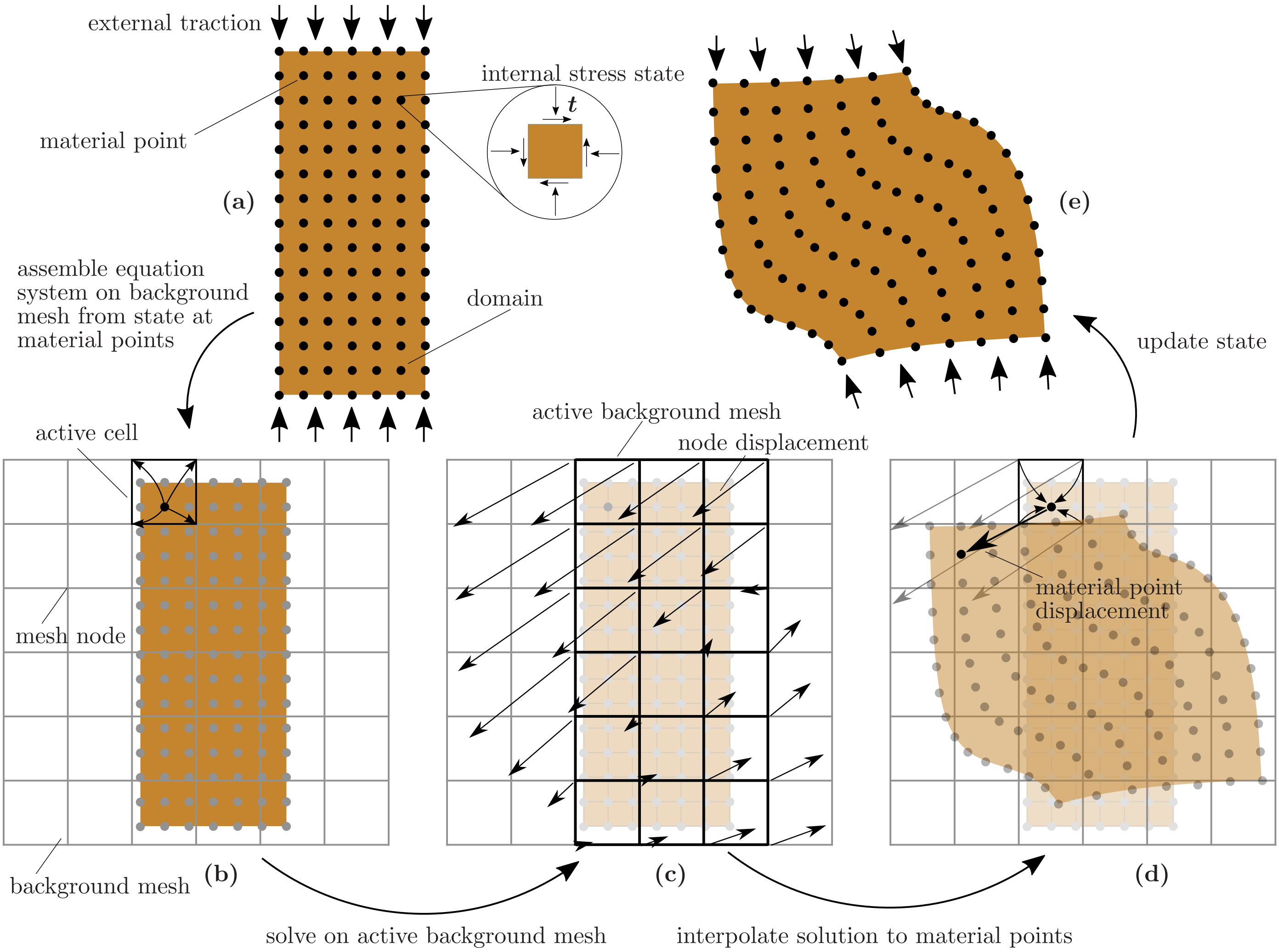

Figure 2: Original material point method: **(a)** a domain is discretized using a finite number of material points, **(b)** in each time step, the global system of equations is assembled by passing information (e.g., momentum) from the material points to a background mesh using an interpolation operation, **(c)** only active cells, i.e., cells with material points located inside, contribute to the global system of equations, **(d)** after solving the global system of equations, the updated solution is interpolated back to the material points, and **(e)** material points positions and deformation state are updated.

necessitate a suitable parametrization, which has yet to be thoroughly investigated in the context of the MPM. Additionally, the robustness of the MPM under excessive shear deformations in micropolar continua, as for instance observed in localized shear bands, has not yet been studied.

This work is motivated by these shortcomings, as well as the promising potential of a gradient-enhanced micropolar theory discussed earlier. In particular, we present an improved numerical method, namely an efficient and robust extension of the iMPM to the gradient-enhanced microplar continuum, denoted here as gradient-enhanced micropolar iMPM (**gmp-iMPM**), for describing complex and extreme deformations under localized material failure in gradient-enhanced micropolar continua in a geometrically exact, three dimensional setting.

The outline of the paper is as follows. In Section 2, we present a formulation of the iMPM for the gradient-enhanced micropolar continuum, aiming at the simulation of strongly localized, inelastic deformations upon material failure resulting in shear bands. In particular, we highlight an efficient numerical implementation using B-splines to overcome well known issues related to cell crossing and locking. For validating the proposed approach, we present a 2D and 3D numerical study in Section 3, together with a comparison with the classical Lagrangian FEM. In Section 4, we conclude with a summary and an outlook on future research activities.

2. A B-spline based gradient-enhanced micropolar implicit material point method

In the following, first, we briefly describe the gradient-enhanced micropolar continuum framework for finite inelastic deformations developed in [60], and its weak form. Next, a B-spline based material point method for the solution of initial boundary value problems (IBVP) is introduced in Section 2.3. Furthermore, the numerical implementation of the formulation is covered, including approaches for handling MPM specific challenges, i.e., the imposition of essential and natural boundary conditions, as well as the tracing of material points in the background mesh. We use the notation used by Eringen [27], employing the index notation due to the nonsymmetry of all involved tensors, using subscripts $(\bullet)_i$ for components and omitting base vectors for readability. We imply summation over repeated subscript indices. Furthermore $(\bullet)_{i,j}$ represents the spatial derivative, and $\dot{(\bullet)} = \frac{\mathrm{D}(\bullet)}{\mathrm{D}t}$ designates the material time derivative of a tensor.

2.1. Gradient-enhanced micropolar continuum framework for large localized inelastic deformations

For the combined gradient-enhanced micropolar continuum each material particle of a body with an initial undeformed volume V^0 and volume $V(t)$ in the current deformed configuration is endowed with three independent variables: (i) the classical displacement field u_i, (ii) an independent field describing the microscopic deformation state in terms of a microscopic orthogonal tensor χ_{iI} [28], and (iii) an additional scalar field $\tilde{\alpha}$ describing the integrity of the material. The current position of a particle

$$x_i = X_I \, \delta_{iI} + u_i \, , \tag{1}$$

with initial position X_I and with δ_{iI} denoting the Kronecker delta, is characterized by the displacement field u_i. Unlike the classical continuum, in addition to the classical macroscopic deformation gradient

$$F_{iI} = x_{i,I} \, , \tag{2}$$

the independent microscopic orthogonal tensor χ_{iI}

$$\chi_{iI}\chi_{jI} = \delta_{ij} \, , \tag{3}$$

characterizes the deformation state. Due to the orthogonal property of χ_{iI}, it can be expressed using a three parameter representation in terms of the axial vector w_i and the Euler-Rodrigues formula

$$\chi_{iI} = \cos(w) \, \delta_{iI} - \sin(w) \, \epsilon_{ijk} \, n_k \, \delta_{jI} + (1 - \cos(w)) n_i \, n_j \delta_{jI} \, , \tag{4}$$

where

$$n_i = w_i / w \quad \text{and} \quad w = \sqrt{w_i \, w_i} \, , \tag{5}$$

with ϵ_{ijk} denoting the Levi-Civita permutation symbol.

The balance equations of the gradient-enhanced micropolar continuum in the quasi-static case, neglecting volumetric couple forces, consist of the balance of linear momentum

$$t_{ij,i} + \rho \, f_j = 0 \quad \text{in } V(t) \, , \tag{6}$$

and the balance of angular momentum

$$m_{ij,i} + \epsilon_{jkl} \, t_{kl} = 0 \quad \text{in } V(t) \, , \tag{7}$$

in which t_{ij} is the macroscopic, in general nonsymmetric, Cauchy stress tensor, m_{ij} is the nonsymmetric couple stress tensor, ρ is the mass density, f_j is the body force per unit mass. The third balance equation is the second order partial differential equation [64]

$$\tilde{\alpha} - l_{\mathrm{d}}^2 \left(\tilde{\alpha}_{,I}\right)_{,I} = \alpha_{\mathrm{d}} \quad \text{in } V^0 \,. \tag{8}$$

This equation describes the nonlocal character of material damage using the independent, damage related field $\tilde{\alpha}$, with the local internal state variable α_{d} acting as the driving force. The domain of nonlocal interaction is related to the length scale parameter l_{d}, which is considered as a material property [3].

2.2. Weak form and spatial discretization

For solving the coupled system of partial differential equations numerically, the weak form is constructed from the three balance equations (6), (7) and (8). To this end, these equations are multiplied by test functions δu_i, δw_i and $\delta\tilde{\alpha}$. Integration over the spatial domain and subsequent application of the Gauss theorem yields the following weak form of the governing equations

$$\int_{V(t)} \delta u_{j,i}\, t_{ij}\, \mathrm{d}V(t) - \int_{V(t)} \delta u_j\, f_j\, \rho\, \mathrm{d}V(t) - \int_{\bar{A}^{\mathrm{t}}(t)} \delta u_j\, \bar{t}_j\, \mathrm{d}\bar{A}^{\mathrm{t}}(t) = 0\,, \tag{9}$$

$$\int_{V(t)} -\delta w_{j,i}\, m_{ij} + \delta w_j\, \epsilon_{jkl}\, t_{kl}\, \mathrm{d}V(t) = 0\,, \tag{10}$$

$$\int_{V^0} \delta\tilde{\alpha}\, \tilde{\alpha} + l_{\mathrm{d}}^2\, \delta\tilde{\alpha}_{,I}\, \tilde{\alpha}_{,I} - \delta\tilde{\alpha}\, \alpha_{\mathrm{d}}\, \mathrm{d}V^0 = 0\,, \tag{11}$$

with $\bar{t}_j$ denoting the surface traction vector acting on the boundary $\bar{A}^{\mathrm{t}}(t)$.

Similar to the FEM, in the MPM a spatial discretization is performed, where the independent fields are interpolated using a finite number of values at the nodes of the background mesh based on a set of suitable shape functions. In contrast to the Lagrangian FEM, this discretization is performed on a rigid, non-deforming background mesh. Accordingly, nodes of the background mesh are not directly associated with the deforming body $V(t)$, and the concept of *total nodal values* is non-existent in the MPM. Furthermore, compared to the FEM, due to alternating computations of *Lagrangian phases*, i.e., the incremental solution on the background mesh, and *convective phases*, i.e., the update of the material points' positions in the background mesh, the MPM inevitably introduces a time discretization. In the following, we focus on a single time increment Δt to the current time t, defining a time interval $[t_{(\mathrm{old})}, t = t_{(\mathrm{old})} + \Delta t]$ with $t_{(\mathrm{old})}$ denoting the previously solved time instant with a completely known state.

During the *Lagrangian phase*, the primary unknowns to be solved for are the *incremental nodal values*, with the frame of reference being the configuration at the previous time instant $t_{(\mathrm{old})}$. During such a time increment, the field solution increments and their derivatives are interpolated using background mesh shape functions $\mathbf{N}_A$ and their derivatives $\mathbf{N}_{A,\tilde{I}}$ with respect to the *undeformed* mesh coordinates, with subscripts $(\bullet)_A$ and $(\bullet)_B$ henceforth denoting node indices of the background mesh as

$$\begin{aligned}
\Delta u_i &= \mathbf{N}_A\, \Delta\mathbf{q}^{\mathrm{u}}{}_{Ai}\,, & \Delta u_{i,\tilde{J}} &= \mathbf{N}_{A,\tilde{J}}\, \Delta\mathbf{q}^{\mathrm{u}}{}_{Ai}\,, \\
\Delta w_i &= \mathbf{N}_A\, \Delta\mathbf{q}^{\mathrm{w}}{}_{Ai}\,, & \Delta w_{i,\tilde{J}} &= \mathbf{N}_{A,\tilde{J}}\, \Delta\mathbf{q}^{\mathrm{w}}{}_{Ai}\,, \\
\Delta\tilde{\alpha} &= \mathbf{N}_A\, \Delta\mathbf{q}^{\alpha}{}_{A}\,, & \Delta\tilde{\alpha}_{,\tilde{I}} &= \mathbf{N}_{A,\tilde{I}}\, \Delta\mathbf{q}^{\alpha}{}_{A}\,.
\end{aligned} \tag{12}$$

Therein, $\Delta\mathbf{q}^{\mathrm{u}}{}_{Ai}$, $\Delta\mathbf{q}^{\mathrm{w}}{}_{Ai}$ and $\Delta\mathbf{q}^{\alpha}{}_{A}$ denote the incremental values of the background mesh nodes of the displacement field u_i, the microrotation field in terms of the components of the axial vector w_i, and the field of the damage-driving variable $\tilde{\alpha}$, respectively. In particular, for parametrizing the microrotations, we adopt the approach used in [60, 25], updating the axial vector w_i incrementally in an additive manner, which leads to a multiplicative update of χ_{iI}. Furthermore, in the present work, for the sake of simplicity we assume an identical interpolation for all fields. Accordingly, the test functions δu_i, δw_i and $\delta\tilde{\alpha}$, and their respective gradients are similarly interpolated using the same interpolation operators $\mathbf{N}_A$ and $\mathbf{N}_{A,\tilde{J}}$, and the respective nodal test values $\delta\mathbf{q}^{\mathrm{u}}{}_{Aj}$, $\delta\mathbf{q}^{\mathrm{w}}{}_{Aj}$, and $\delta\mathbf{q}^{\alpha}{}_{A}$.

Note that, as a result of the convective phase, the undeformed mesh coordinates $\tilde{X}_{\tilde{I}}$ coincide with the particle coordinates at the end of the previously converged time instant $t_{(\mathrm{old})}$, i.e.,

$$\tilde{X}_{\tilde{I}} \leftarrow x_i(t_{(\mathrm{old})})\,\delta_{i\tilde{I}} \tag{13}$$

at the end of each time step.

Following this concept, the total deformation gradient F_{iI} is decomposed in a multiplicative manner

$$F_{iI} = \tilde{F}_{i\tilde{I}}\, F^{(\mathrm{old})}{}_{\tilde{I}I}\,, \tag{14}$$

with

$$F^{(\mathrm{old})}{}_{\tilde{I}I} = \frac{\partial \tilde{X}_{\tilde{I}}}{\partial X_I} = \frac{\partial x_i(t_{(\mathrm{old})})\,\delta_{i\tilde{I}}}{\partial X_I} \tag{15}$$

denoting the previously converged total deformation gradient at time $t_{(\mathrm{old})}$, which is treated as a history variable, and the incrementally updating deformation gradient $\tilde{F}_{i\tilde{I}}$ which follows as

$$\tilde{F}_{i\tilde{I}} = \Delta u_{i,\tilde{I}} + \delta_{i\tilde{I}} = \mathbf{N}_{A,\tilde{I}}\,\Delta\mathbf{q}^{\mathrm{u}}{}_{Ai} + \delta_{i\tilde{I}}\,. \tag{16}$$

Utilizing this decomposition, the derivatives of the shape function with respect to the current, deformed configuration, and the materially undeformed configuration can be expressed as

$$\mathbf{N}_{A,i} = \mathbf{N}_{A,\tilde{I}}\,(\tilde{F})^{-1}{}_{\tilde{I}i}\,, \tag{17}$$

$$\mathbf{N}_{A,I} = \mathbf{N}_{A,\tilde{I}}\,(\tilde{F})^{-1}{}_{\tilde{I}i}\,F_{iI}\,. \tag{18}$$

This allows, using the Kirchhoff stress $\tau_{ij} = J\,t_{ij}$ and the Kirchhoff couple stress $\mu_{ij} = J\,m_{ij}$ for convenience, to express the discretized weak form as

$$\delta\mathbf{q}^{\mathrm{u}}{}_{Aj}\left(\int_{V^0} \mathbf{N}_{A,i}\,\tau_{ij}\,\mathrm{d}V^0 - \int_{V^0} \mathbf{N}_A\,f_j\,\rho_0\,\mathrm{d}V^0 - \int_{\bar{A}^{\mathrm{t}}(t)} \mathbf{N}_A\,\bar{t}_j\,\mathrm{d}\bar{A}^{\mathrm{t}}(t)\right) = \delta\mathbf{q}^{\mathrm{u}}{}_{Aj}\,\mathbf{r}^{\mathrm{u}}{}_{Aj} = 0\,, \tag{19}$$

$$\delta\mathbf{q}^{\mathrm{w}}{}_{Aj}\int_{V^0} -\mathbf{N}_{A,i}\,\mu_{ij} + \mathbf{N}_A\,\epsilon_{jkl}\,\tau_{kl}\,\mathrm{d}V^0 = \delta\mathbf{q}^{\mathrm{w}}{}_{Aj}\,\mathbf{r}^{\mathrm{w}}{}_{Aj} = 0\,, \tag{20}$$

$$\delta\mathbf{q}^{\alpha}{}_{A}\int_{V^0} \mathbf{N}_A\,\tilde{\alpha} + (l_{\mathrm{d}})^2\,\mathbf{N}_{A,I}\,\tilde{\alpha}_{,I} - \mathbf{N}_A\,\alpha_{\mathrm{d}}\,\mathrm{d}V^0 = \delta\mathbf{q}^{\alpha}{}_{A}\,\mathbf{r}^{\alpha}{}_{A} = 0, \tag{21}$$

in which use of the Jacobian determinant

$$J = \frac{\mathrm{d}V(t)}{\mathrm{d}V^0} = \frac{\rho_0}{\rho} = \det F_{iI} \tag{22}$$

was made to transform the volume integrals to the undeformed configuration, and with $\mathbf{r}^{\mathrm{u}}{}_{Aj}$, $\mathbf{r}^{\mathrm{w}}{}_{Aj}$ and $\mathbf{r}^{\alpha}{}_{A}$ denoting the nodal residual vectors, forming the system of nonlinear equations. Expressing the constitutive relations in terms of the Kirchhoff stress measures is particularly convenient for efficient numerical implementations, as the resulting expressions become independent of the Jacobian determinant J.

In equations (19), (20) and (21), the Kirchhoff stress τ_{ij}, the Kirchhoff couple stress μ_{ij} and local damage driving variable α_d are functions of F_{iI}, w_i, $w_{i,I}$, $\tilde{\alpha}$, and a material specific set of thermodynamic internal state variables $\alpha_\bullet$, i.e.,

$$\tau_{ij} = \tau_{ij}\,(F_{iI}\,, w_i, w_{i,I}, \tilde{\alpha}, \alpha_\bullet)\,, \quad \mu_{ij} = \mu_{ij}(F_{iI}\,, w_i, w_{i,I}, \tilde{\alpha}, \alpha_\bullet)\,, \quad \alpha_\mathrm{d} = \alpha_\mathrm{d}(F_{iI}\,, w_i, w_{i,I}, \tilde{\alpha}, \alpha_\bullet)\,. \tag{23}$$

Accordingly, they depend on the incremental node values $\Delta\mathbf{q}^\mathrm{u}{}_{Bk}$, $\Delta\mathbf{q}^\mathrm{w}{}_{Bk}$ and $\Delta\mathbf{q}^\alpha{}_B$, and the loading history of the material.

2.3. Material point method for solving the IBVP

For the classical MPM, considering material points as concentrated, shapeless point masses, the spatial domain occupied by the body $V(t)$ is discretized by a finite number N of material points with positions $(x_p)_i$

$$V(t) = \int_{V(t)} \mathrm{d}V(t) \approx \sum_p^N V_p(t) \; = \sum_p^N J_p V_p^0\,, \tag{24}$$

and we henceforth use the subscript $(\bullet)_p$ for designating an individual material point. Furthermore, $V_p(t)$ and V_p^0 denote the current and initial volume of each material point, and J_p denotes the determinant of the material point's deformation gradient $(F_{iI}\,)_p$.

As the final step for the MPM, envisioning the material points as convecting quadrature points, the volume integrals in equations (19), (20) and (21) are approximated by

$$\int_{V^0} \mathbf{N}_{A,i}\,\tau_{ij}\,\mathrm{d}V^0 - \int_{V^0} \mathbf{N}_A\,f_j\,\rho_0\,\mathrm{d}V^0 \approx \sum_p^N \mathbf{N}_{A,i}\,\tau_{ij}\;V_p^0 - \sum_p^N \mathbf{N}_A\,f_j\,\rho_0\,V_p^0\,, \tag{25}$$

$$\int_{V^0} -\mathbf{N}_{A,i}\,\mu_{ij} + \mathbf{N}_A\,\epsilon_{jkl}\,\tau_{kl}\,\mathrm{d}V^0 \approx \sum_p^N \left(-\mathbf{N}_{A,i}\,\mu_{ij} + \mathbf{N}_A\,\epsilon_{jkl}\,\tau_{kl}\right)\,V_p^0\,, \tag{26}$$

$$\int_{V^0} \mathbf{N}_A\,\tilde{\alpha} + (l_\mathrm{d})^2\,\mathbf{N}_{A,I}\,\tilde{\alpha}_{,I} - \mathbf{N}_A\,\alpha_\mathrm{d}\,\mathrm{d}V^0 \approx \sum_p^N \left(\mathbf{N}_A\,\tilde{\alpha} + (l_\mathrm{d})^2\,\mathbf{N}_{A,I}\,\tilde{\alpha}_{,I} - \mathbf{N}_A\,\alpha_\mathrm{d}\right)\,V_p^0\,, \tag{27}$$

in which the explicit dependence of $\tau_{ij} = (\tau_{ij})_p$, $\mu_{ij} = (\mu_{ij})_p$, $\alpha_\mathrm{d} = (\alpha_\mathrm{d})_p$, $\tilde{\alpha} = (\tilde{\alpha})_p$ $\mathbf{N}_A = \mathbf{N}_A((\tilde{X}_p)_{\tilde{I}})$ and $\mathbf{N}_{A,\tilde{I}} = \mathbf{N}_{A,\tilde{I}}((\tilde{X}_p)_{\tilde{I}})$ on the material point and its location $(\tilde{X}_p)_{\tilde{I}}$ was omitted for the sake of readability. Note that, similar to the Lagrangian FEM, during the Lagrangian phase the relative position of the material points with respect to the background mesh remains fixed, i.e., during this phase the background mesh is moving and deforming with the body, and hence $(\tilde{X}_p)_{\tilde{I}}$ is constant during the Lagrangian phase.

One particularly appealing characteristic of the MPM is its continuum based nature, which allows adaptation of sophisticated continuum based constitutive models, e.g., those developed in the context of the FEM. The gmp-iMPM has been formulated in such a way that the constitutive models and stress update algorithms developed previously in [60, 57, 23] for use in the FEM can be readily adopted.

The system of nonlinear equations formed by the three residual vectors $\mathbf{r}^\mathrm{u}{}_{Aj}$, $\mathbf{r}^\mathrm{w}{}_{Aj}$ and $\mathbf{r}^\alpha{}_A$ is commonly solved by means of the Newton-Raphson scheme, which requires the derivatives of those residual vectors with respect to the vectors of the incremental nodal values. Those derivatives are summarized in Section 2.6.

Once the updated increments of the nodal solution have been computed, the Lagrangian phase is finished and is then followed by the convective phase, in which the positions of the material points $x_i(t) = X_{\tilde{I}}\,\delta_{i\tilde{I}} + \Delta u_i$ are accepted as converged, the deformed background mesh is reset, and the current time t is accepted as the previously converged time instant $t_{(\mathrm{old})}$, i.e., $t_{(\mathrm{old})} \leftarrow t$.

2.4. B-spline shape functions

While traditionally classical linear shape functions have been used for the MPM, the use of higher order B-spline shape functions, which are commonly employed in the Isogeometric FEM, has gained a certain popularity, as they allow to overcome the well known issues related to cell crossing of material points due to their higher order continuity. Moreover, they are less prone to locking behavior upon plastic deformations, as will be demonstrated in Section 3.

In one dimension, the value of a B-spline of order ζ associated with node A of the background mesh (commonly denoted as *control point* in Isogeometric FEM terminology) is expressed recursively as

$$B_A^{\zeta}(X) = \frac{X - \xi_A}{\xi_{A+\zeta} - \xi_A}\, B_A^{\zeta-1}(X) + \frac{\xi_{A+\zeta+1} - X}{\xi_{A+\zeta+1} - \xi_{A+1}}\, B_{A+1}^{\zeta-1}(X) \tag{28}$$

with

$$B_A^0(X) = \begin{cases} 1, & \text{if } \xi_A \leq X < \xi_{A+1} \\ 0, & \text{otherwise}\,, \end{cases} \tag{29}$$

and with ξ_A denoting the A^{th} *knot* from a predefined set of *knots* $\{\xi_1, \xi_2, ..., \xi_{\mathrm{M}+(\zeta)+1}\}$, which controls the supports of the in total M B-spline functions. This concept can be generalized to multiple spatial dimensions D using products of B-spline basis functions. Thus, for obtaining the shape functions $\mathbf{N}_A$ of chosen degree ζ at location $\tilde{X}_{\tilde{I}}$, the index A of the mesh node is associated with a cartesian triple index (A_1, A_2, A_3), A_d denoting the index of the B-spline basis function in direction d. The shape function $\mathbf{N}_A$ is then defined as the product of the B-spline basis functions in the D spatial directions, each of which is evaluated for the respective coordinate $(\tilde{X}_{\tilde{I}})_d$ of $\tilde{X}_{\tilde{I}}$, i.e.

$$\mathbf{N}_A(\tilde{X}_{\tilde{I}}) = \prod_{d=1}^{\mathrm{D}} B_{A_d}^{\zeta}((\tilde{X}_{\tilde{I}})_d)\,. \tag{30}$$

For the numerical implementation, identical to the FEM due to the bounded support of each shape function, the evaluation of residuals and stiffness is performed by partitioning the approximations (25), (26) and (27) of the total integrals into a finite number of *cells*, with each cell being associated with a certain number of nodes and knots of the background mesh, depending on the chosen order ζ. Only active cells, i.e., cells hosting material points are considered for the assembly of the global system of equations, which follows the standard assembly procedure.

2.5. Boundary conditions and constraints

Compared to the Lagrangian FEM, a particular challenge in the MPM is the imposition of Dirichlet boundary conditions on surfaces which do not conform with the background mesh. For this purpose, we propose the use of weakly imposed boundary conditions based on a penalty formulation, as developed in [9]. For the sake of brevity, we restrict the discussion to boundary conditions for the displacement field in the following.

For imposing Dirichlet boundary conditions on a set of N^{u} material points forming a surface $\bar{A}_p^{\mathrm{u}}(t)$, the residual vector $\mathbf{r}^{\mathrm{u}}{}_{Ai}$ is augmented by the penalty term

$$\sum_p^{N^{\mathrm{u}}} \mathbf{N}_A\, \gamma_{\mathrm{p}}\, ((u_p)_j - \bar{u}_j)\, V_p(t)\,. \tag{31}$$

with γ_{p} as the penalty parameter, $(u_p)_j = \mathbf{N}_A\, \boldsymbol{\Delta}\mathbf{q}^{\mathrm{u}}{}_{Aj} + (u_p(t_{(\mathrm{old})}))_j$ as the current material point displacement, and with $\bar{u}_j$ denoting the prescribed displacement. In a similar manner, constraints can be formulated, e.g., coupling one displacement component of a material point to the respective average over a surface for, e.g., formulating rigid body constraints.

For prescribing Neumann boundary conditions, i.e., surface tractions acting on a deforming surface $\bar{A}^{\mathrm{t}}(t)$, the surface integral in (19) is approximated as

$$\int_{\bar{A}^{\mathrm{t}}(t)} \mathbf{N}_A \, \bar{t}_j \, \mathrm{d}\bar{A}^{\mathrm{t}}(t) \approx \sum_p^{N^{\mathrm{t}}} \mathbf{N}_A \, \bar{t}_j \, \bar{A}^{\mathrm{t}}_p(t) \tag{32}$$

using the set of N^{t} material points at the boundary, with $\bar{A}^{\mathrm{t}}_p(t)$ denoting the surface area associated with the material point in the deformed configuration. Relating this equation to the undeformed configuration, exploiting Nanson's formula, leads to

$$\bar{t}_j \, \bar{A}^{\mathrm{t}}_p(t) = J \, {F^{-1}}_{Jj} \, \bar{T}_J \, \bar{A}^{\mathrm{t},0}_p \tag{33}$$

with $\bar{T}_J$ denoting the initial surface traction vector, and $\bar{A}^{\mathrm{t},0}_p$ as the area associated with the material point in the undeformed configuration.

In principle, both weakly imposed Dirichlet boundary conditions (31) and Neumann boundary conditions (32) could be enforced using sets of *dummy* surface material points which form a denser representation of the respective surfaces and which are not used for computing the volume integrals in (25), (26) and (27). This method is described in [9], but not pursued in the present work.

2.6. Tangent operators

For solving the global system of nonlinear equations using the Newton-Raphson method, the global stiffness matrix is assembled from the derivatives of the nodal residual vectors, i.e., of ${\mathbf{r}^{\mathrm{u}}}_{Aj}$ in the form

$$\frac{\partial {\mathbf{r}^{\mathrm{u}}}_{Aj}}{\partial \Delta {\mathbf{q}^{\mathrm{u}}}_{Bk}} = \sum_p^N \left(\mathbf{N}_{A,i} \, \frac{\partial \tau_{ij}}{\partial F_{mM}} \, \frac{\partial F_{mM}}{\partial \tilde{F}_{k\tilde{K}}} \, \mathbf{N}_{B,\tilde{K}} - \mathbf{N}_{A,k} \, \mathbf{N}_{B,i} \, \tau_{ij} \right) V^0_p \tag{34}$$

$$- \sum_p^N \mathbf{N}_A \, \bar{t}_i \left(\delta_{ij}\delta_{lk} - \delta_{ik}\delta_{lj} \right) \mathbf{N}_{B,l} \, \bar{A}^{\mathrm{t}}_p(t) \tag{35}$$

$$\frac{\partial {\mathbf{r}^{\mathrm{u}}}_{Aj}}{\partial \Delta {\mathbf{q}^{\mathrm{w}}}_{Bk}} = \sum_p^N \mathbf{N}_{A,i} \left(\frac{\partial \tau_{ij}}{\partial w_{m,M}} \, \frac{\partial F_{mM}}{\partial \tilde{F}_{k\tilde{K}}} \, \mathbf{N}_{B,\tilde{K}} + \frac{\partial \tau_{ij}}{\partial w_k} \, \mathbf{N}_B \right) V^0_p \,, \tag{36}$$

$$\frac{\partial {\mathbf{r}^{\mathrm{u}}}_{Aj}}{\partial \Delta {\mathbf{q}^{\alpha}}_{B}} = \sum_p^N \mathbf{N}_{A,i} \, \frac{\partial \tau_{ij}}{\partial \tilde{\alpha}} \, \mathbf{N}_B \, V^0_p \,, \tag{37}$$

of ${\mathbf{r}^{\mathrm{w}}}_{Aj}$ as

$$\frac{\partial {\mathbf{r}^{\mathrm{w}}}_{Aj}}{\partial \Delta {\mathbf{q}^{\mathrm{u}}}_{Bk}} = \sum_p^N \left(-\mathbf{N}_{A,i} \, \frac{\partial \mu_{ij}}{\partial F_{mM}} \, \frac{\partial F_{mM}}{\partial \tilde{F}_{k\tilde{K}}} \, \mathbf{N}_{B,\tilde{K}} + \mathbf{N}_A \, \epsilon_{jmn} \, \frac{\partial \tau_{mn}}{\partial F_{lL}} \, \frac{\partial F_{lL}}{\partial \tilde{F}_{k\tilde{K}}} \, \mathbf{N}_{B,\tilde{K}} + \mathbf{N}_{A,k} \, \mathbf{N}_{B,i} \, \mu_{ij} \right) \; V^0_p \,, \tag{38}$$

$$\frac{\partial {\mathbf{r}^{\mathrm{w}}}_{Aj}}{\partial \Delta {\mathbf{q}^{\mathrm{w}}}_{Bk}} = \sum_p^N \left(-\mathbf{N}_{A,i} \left(\frac{\partial \mu_{ij}}{\partial w_{m,M}} \, \frac{\partial F_{mM}}{\partial \tilde{F}_{k\tilde{K}}} \, \mathbf{N}_{B,\tilde{K}} + \frac{\partial \mu_{ij}}{\partial w_k} \, \mathbf{N}_B \right) \right. \tag{39}$$

$$\left. + \mathbf{N}_A \, \epsilon_{jmn} \left(\frac{\partial \tau_{mn}}{\partial w_{l,L}} \, \frac{\partial F_{lL}}{\partial \tilde{F}_{k\tilde{K}}} \, \mathbf{N}_{B,\tilde{K}} + \frac{\partial \tau_{mn}}{\partial w_k} \, \mathbf{N}_B \right) \right) \; V^0_p \,, \tag{40}$$

$$\frac{\partial {\mathbf{r}^{\mathrm{w}}}_{Aj}}{\partial \Delta {\mathbf{q}^{\alpha}}_{B}} = \sum_p^N \left(-\mathbf{N}_{A,i} \, \frac{\partial m_{ij}}{\partial \tilde{\alpha}} \, \mathbf{N}_B + \mathbf{N}_A \, \epsilon_{jmn} \, \frac{\partial \tau_{mn}}{\partial \tilde{\alpha}} \, \mathbf{N}_B \right) \; V^0_p \,, \tag{41}$$

and of ${\mathbf{r}^\alpha}_A$ as

$$\frac{\partial {\mathbf{r}^\alpha}_A}{\partial \Delta {\mathbf{q}^{\mathrm{u}}}_{Bk}} = \sum_p^N \left(-\mathbf{N}_A \, \frac{\partial \alpha_{\mathrm{d}}}{\partial F_{mM}} \, \frac{\partial F_{mM}}{\partial \tilde{F}_{k\tilde{K}}} \, \mathbf{N}_{B,\tilde{K}} \right) V_p^0 \,, \tag{42}$$

$$\frac{\partial {\mathbf{r}^\alpha}_A}{\partial \Delta {\mathbf{q}^{\mathrm{w}}}_{Bk}} = \sum_p^N -\mathbf{N}_A \left(\frac{\partial \tilde{\alpha}}{\partial w_{m,M}} \, \frac{\partial F_{mM}}{\partial \tilde{F}_{k\tilde{K}}} \, \mathbf{N}_{B,\tilde{K}} + \frac{\partial \tilde{\alpha}}{\partial w_k} \, \mathbf{N}_B \right) V_p^0 \,, \tag{43}$$

$$\frac{\partial {\mathbf{r}^\alpha}_A}{\partial \Delta {\mathbf{q}^\alpha}_B} = \sum_p^N \left(\mathbf{N}_A \, \mathbf{N}_B + l_{\mathrm{d}}^2 \, \mathbf{N}_{A,I} \, \mathbf{N}_{B,I} - \mathbf{N}_A \, \frac{\partial \alpha_{\mathrm{d}}}{\partial \tilde{\alpha}} \, \mathbf{N}_B \right) V_p^0 \,, \tag{44}$$

with respect to $\Delta {\mathbf{q}^{\mathrm{u}}}_{Bk}$, $\Delta {\mathbf{q}^{\mathrm{w}}}_{Bk}$, and $\Delta {\mathbf{q}^\alpha}_B$, using the relation

$$\frac{\partial F_{mM}}{\partial \tilde{F}_{k\tilde{K}}} = \frac{\partial w_{m,M}}{\partial w_{k,\tilde{K}}} = \delta_{mk} \, {F^{(\mathrm{old})}}_{\tilde{K}M} \,. \tag{45}$$

Furthermore, $\frac{\partial \tau_{ij}}{\partial F_{kK}}$, $\frac{\partial \tau_{ij}}{\partial w_k}$, $\frac{\partial \tau_{ij}}{\partial w_{k,K}}$, $\frac{\partial \tau_{ij}}{\partial \tilde{\alpha}}$, $\frac{\partial \mu_{ij}}{\partial F_{kK}}$, $\frac{\partial \mu_{ij}}{\partial w_k}$, $\frac{\partial \mu_{ij}}{\partial w_{k,K}}$, $\frac{\partial \mu_{ij}}{\partial \tilde{\alpha}}$, $\frac{\partial \alpha_{\mathrm{d}}}{\partial F_{kK}}$, $\frac{\partial \alpha_{\mathrm{d}}}{\partial w_k}$, $\frac{\partial \alpha_{\mathrm{d}}}{\partial w_{k,K}}$, and $\frac{\partial \alpha_{\mathrm{d}}}{\partial \tilde{\alpha}}$ denote the consistent tangent operators at the constitutive level, which are consistently computed as part of the stress update algorithm [60, 24].

2.7. Fast tracing of material points in the background mesh using a k-d tree algorithm.

Unlike in the FEM, where the numerical integration is performed using quadrature points that are directly associated with a single finite element, the material points in the context of the MPM may change cells in the rigid background mesh. Accordingly, prior to each time step, the connectivity between material points and the background mesh has to be determined and each material point has to be associated with its hosting background cell. The most trivial approach for locating material points in the background mesh would be a loop over all material points in which a loop over all background cells is performed until the background cell covering each material point is found. Of course, this brute force approach is not feasible for problems involving a large number of material points and background cells. To overcome this issue a k-d tree is employed for the fast material point tracing. The use of a k-d tree in the present context includes the following three main parts, which are illustrated in Fig. 3 and explained in the following:

(i) ***k*-d tree setup (Fig. 3, top row)**
Prior to the start of the simulation, the k-d tree is initialized. Thereby, the entire computational domain, which is covered by the background mesh, is partitioned into k-d tree boxes. For a given number of levels, the resulting subdomains are again divided until level 0 is attained, cf. Fig. 3 (top row). Then, all background cells, which are (at least partially) included in a k-d tree box are assigned to the latter. Note that a background mesh cell is partially covered if at least one vertex is inside of the k-d tree box. The assignment of background mesh cells to k-d tree boxes must be performed only once since the background mesh is rigid, and therefore the connectivity between background cells and k-d tree boxes does not change during the simulation.

(ii) **Initial assignment of material points in the background mesh (Fig. 3, mid row)**
After the setup of the k-d tree, an initial assignment of the material points (undeformed configuration) in the k-d tree, and subsequently, the assignment to the respective background cells is performed. This includes a search downwards the k-d tree until level 0 is reached, and subsequently, the assignment to the background cell. For each material point, the respective background cell is stored as an initial guess for a tracing in the deformed configuration. This step is performed only once before the simulation.

(iii) **Tracing of material points in the background mesh (Fig. 3, bottom row)**
During the simulation the material points move with respect to the background mesh, which makes a tracing of the material points necessary at the beginning of each time step. The tracing process starts with a verification if the respective material point is still within the background cell it was associated with in the previous time instant. For small deformations, this is expected to be the case for many material points. However, if a material point has left the previous background cell, instead of repeating the initial assignment with the actual spatial configuration, the previous k-d tree box is utilized as an initial guess for an even faster tracing, cf. Fig. 3. Assuming relatively small deformation increments, it is highly probable that a material point which left a background cell, enters a cell which is in the immediate surrounding area. If the material point is not covered in the initially guessed k-d tree cell, the search is performed recursively upwards the tree beginning with the parent of the latter. Once a box containing the material point is found, the search is performed downwards again until level 0 is attained, following step (ii). This approach for tracing material points has proven to be efficient if the time steps are small, which is usually the case for highly nonlinear problems.

2.8. Summary of the gmp-iMPM

Algorithm 1 summarizes the proposed gmp-iMPM, showing the performed computations.

Algorithm 1 GMP-IMPM

procedure PREPROCESSING
  $V^0 \approx \sum_p^N V_p^0$, ▷ Populate material points to cover V^0, cf. Eq. (24)
  SETUP BACKGROUND MESH
  SETUP K-D TREE ▷ Initial partitioning of the computational domain; cf. Section 2.7
end procedure
procedure TRANSIENT ANALYSIS
  for all Δt **do**
    $t \leftarrow t_{(\text{old})} + \Delta t$ ▷ Define time step
    $\mathbf{N}_A(\tilde{X}_{\tilde{I}}), \mathbf{N}_{A,\tilde{I}}(\tilde{X}_{\tilde{I}}) \leftarrow$ MATERIAL POINT TRACING ▷ Locate material point; define active set of cells cf. Section 2.7
    procedure LAGRANGIAN PHASE
      while not converged **do** ▷ Newton Scheme
        Δu_i, Δw_i, $\Delta\tilde{\alpha} \leftarrow \Delta\mathbf{q}^{\text{u}}{}_{Bk}$, $\Delta\mathbf{q}^{\text{w}}{}_{Bk}$, $\Delta\mathbf{q}^{\alpha}{}_{B}$ ▷ Compute field increments for material points, cf. Eq. (12)
        $\tilde{F}_{i\tilde{I}} \leftarrow \Delta u_i$ ▷ Compute incrementally updating deformation gradient
        $F_{iI} \leftarrow \tilde{F}_{i\tilde{I}}\, , F^{(\text{old})}{}_{\tilde{I}I}$ ▷ Update deformation from history, cf. Eq. (14)
        $\tau_{ij}\, , \mu_{ij}$, $\alpha_{\text{d}} \leftarrow F_{iI}\, , w_i, w_{i,I}, \tilde{\alpha}, \alpha_{\bullet}$ ▷ Compute material point response, cf. Eq. (23)
        $\mathbf{r}^{\text{u}}{}_{Aj}$, $\mathbf{r}^{\text{w}}{}_{Aj}$, $\mathbf{r}^{\alpha}{}_{A} \leftarrow \tau_{ij}\, , \mu_{ij}$, α_{d}, $\tilde{\alpha}$ ▷ Compute volumetric kernels contributions: (25), (26), (27)
        $\mathbf{r}^{\text{u}}{}_{Aj}$, $\mathbf{r}^{\text{w}}{}_{Aj}$, $\mathbf{r}^{\alpha}{}_{A} \leftarrow \bar{t}_i, \bar{u}_i$ ▷ Compute boundary conditions and constraints, cf. Eqs. (31), (32)
        $\mathbf{Ax} = \mathbf{b} \leftarrow \mathbf{r}^{\text{u}}{}_{Aj}$, $\mathbf{r}^{\text{w}}{}_{Aj}$, $\mathbf{r}^{\alpha}{}_{A}$ ▷ Assemble global system of equations, cf. Eqs. (19), (20), (21)
        $\Delta\mathbf{q}^{\text{u}}{}_{Bk}$, $\Delta\mathbf{q}^{\text{w}}{}_{Bk}$, $\Delta\mathbf{q}^{\alpha}{}_{B} \leftarrow \mathbf{x}$ ▷ Solve global system for corrections to nodal solution increments
      end while
    end procedure
    procedure CONVECTIVE PHASE
      $t_{(\text{old})} \leftarrow t$ ▷ Advance time
      $\tilde{X}_{\tilde{I}} \leftarrow x_i(t_{(\text{old})})\, \delta_{i\tilde{I}}$ ▷ Reset background mesh and update positions, cf. Eq. (13)
    end procedure
  end for
end procedure

3. Numerical study and comparison with the FEM

The proposed gmp-iMPM is assessed and compared to the FEM in two challenging benchmark examples involving strongly localized, shear band dominated material failure. In detail, we focus on (i) a 2D plane strain compression test on prismatic sandstone specimens, resembling the experiments by Ord et al. [63], and (ii) a 3D triaxial extension test on cylindrical sandstone specimens.

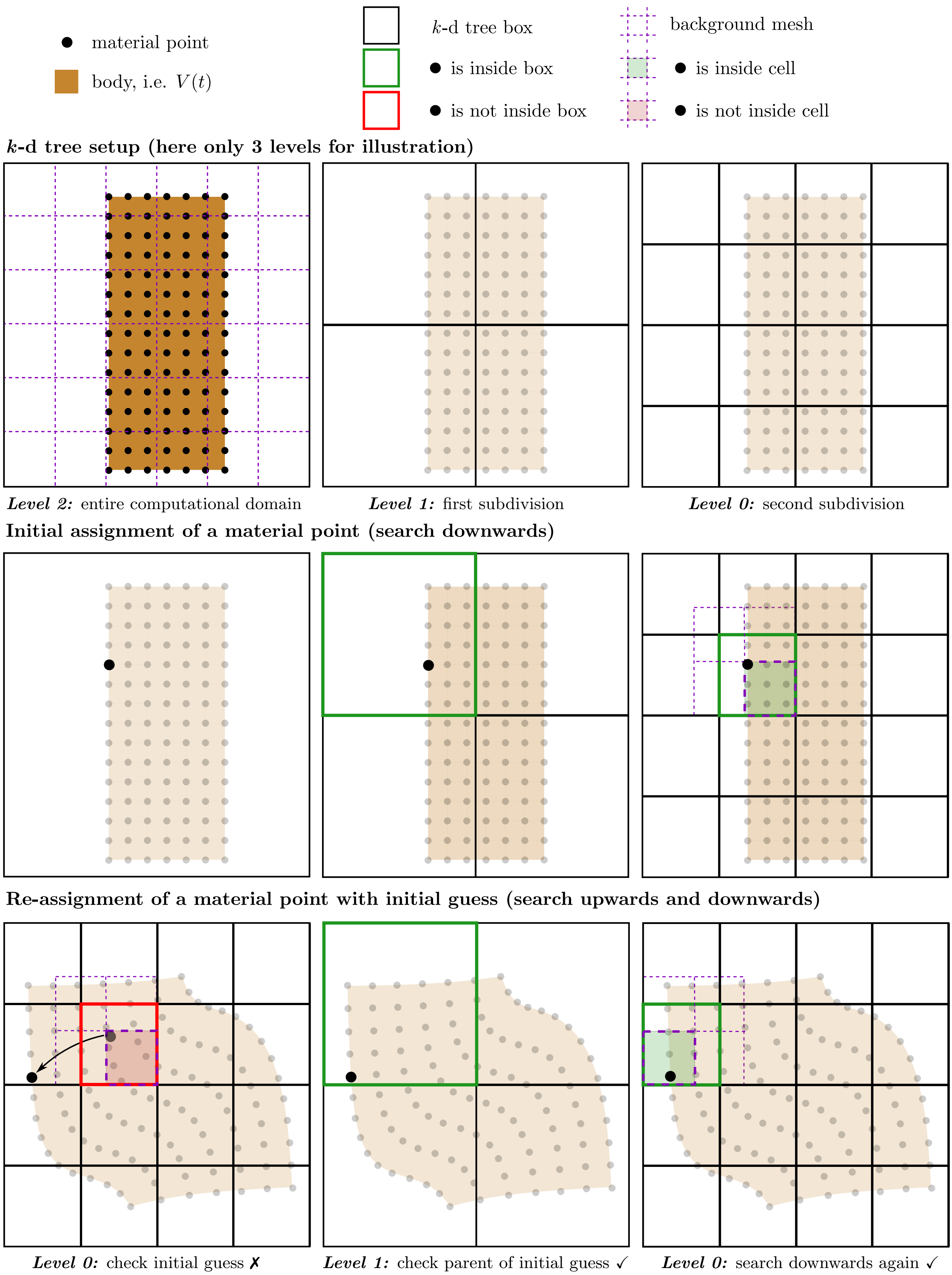

Figure 3: Efficient tracing of material points in the background mesh: initial setup of the k-d tree prior to the start of the simulation (top row), initial assignment of the material points (undeformed reference configuration) using the previously built tree (mid row), and efficient tracing of material points (deformed configuration) using the previous k-d tree box as initial guess and subsequent search upwards and downwards in the tree (bottom row).

For modeling the material behavior of the sandstone, we employ the gradient-enhanced micropolar hyperelastic damage-plastic model for Gosford sandstone proposed in [60], originally developed to be used in the context of the FEM. It is considered as a representative benchmark constitutive model for cohesive-frictional materials, as it accounts for nonlinear, damaging elastic behavior, as well as hardening finite strain plasticity with a pressure dependent yield function. The evolution of gradient-enhanced damage is driven by the accumulation of plastic deformation. The model was developed and calibrated based on the plane strain compression tests on prismatic Gosford sandstone specimens reported in [63], and the good predictive capabilities were demonstrated in [60].

The basic model formulation is summarized briefly in the following, whereas the reader is referred to [60] for a detailed explanation of the model. For the subsequently presented simulations, the gmp-iMPM and the constitutive models are implemented as an extension of the `EdelweissFE` [56] finite element code, using the `Marmot` [22] material library. For performing the numerous higher order tensor contractions efficiently, we make use of the `Fastor` [68] library.

3.1. Material model for Gosford sandstone – summary

For an objective description of a material point, a set of Lagrangian tensors, consisting of the Cosserat deformation tensor

$$\mathfrak{C}_{IJ} = F_{iI}\, \chi_{iJ}\,, \tag{46}$$

and the wryness tensor

$$\Gamma_{KLI} = \chi_{iK}\, \chi_{iL,I}\,, \tag{47}$$

are used. Since the wryness tensor Γ_{KLI} is skew symmetric in its first two indices K and L, an axial representation can be exploited yielding

$$\Gamma_{KLI} = -\epsilon_{JKL}\, \Gamma_{JI}\,. \tag{48}$$

Next, the elastic-plastic split is introduced. First, at the macroscopic level, an elastic-plastic split based on the multiplicative decomposition of the deformation gradient is assumed as

$$F_{iI} = F^{\mathrm{e}}{}_{i\bar{I}} F^{\mathrm{p}}{}_{\bar{I}I}\,, \tag{49}$$

known as the Kröner-Lee decomposition [45, 46], denoting the macroscopic stress free intermediate configuration by the overhead bar [60]. Using the multiplicative decomposition (49), the elastic deformation tensor $\mathfrak{C}^{\mathrm{e}}{}_{\bar{I}J}$ is formed, resulting from the multiplicative decomposition as

$$\mathfrak{C}^{\mathrm{e}}{}_{\bar{I}J} = F^{\mathrm{e}}{}_{i\bar{I}}\, \chi_{iJ} = \left(F^{\mathrm{p}}\right)^{-1}{}_{I\bar{I}}\, \mathfrak{C}_{IJ}\,. \tag{50}$$

Second, for the wryness tensor, an additive decomposition

$$\Gamma_{JI} = \Gamma^{\mathrm{e}}{}_{JI} + \Gamma^{\mathrm{p}}{}_{JI}\,, \tag{51}$$

is assumed. Therein, we denote

$$\Gamma^{\mathrm{e}}{}_{JI} = -\frac{1}{2}\, \epsilon_{JKL}\, \chi_{kK}\, \chi^{\mathrm{e}}{}_{kL,I} \quad \text{and} \quad \Gamma^{\mathrm{p}}{}_{JI} = -\frac{1}{2}\, \epsilon_{JKL}\, \chi_{kK}\, \chi^{\mathrm{p}}{}_{kL,I}\,, \tag{52}$$

by assuming an additive decomposition of the material gradient $\chi_{iJ,K}$ as

$$\chi_{iJ,K} = \chi^{\mathrm{e}}{}_{iJ,K} + \chi^{\mathrm{p}}{}_{iJ,K}\,. \tag{53}$$

For the considered model, the elastic Helmholtz free energy density Ψ^{e} is assumed to be a function of the elastic deformation tensor ${\mathfrak{C}^{\mathrm{e}}}_{\bar{I}J}$, the elastic wryness tensor ${\Gamma^{\mathrm{e}}}_{JI}$, and a scalar isotropic material damage parameter $0 \leq \omega \leq 1$ in the form

$$\Psi^{\mathrm{e}} = \Psi^{\mathrm{e}}({\mathfrak{C}^{\mathrm{e}}}_{\bar{I}J}, {\Gamma^{\mathrm{e}}}_{JI}, \omega)\,. \tag{54}$$

The hyperelastic-plastic relations are formulated in terms of the Biot stress measure $T_{\bar{I}J}$, which is power conjugate to the elastic Cosserat deformation rate ${\dot{\mathfrak{C}}^{\mathrm{e}}}_{\bar{I}J}$, and is defined with respect to both the undeformed and the stress free intermediate configurations as

$$T_{\bar{I}J} = J\,{(F^{\mathrm{e}})^{-1}}_{\bar{I}i}\, t_{ij}\, \chi_{jJ}\,. \tag{55}$$

Furthermore, the Mandel stress measure $\mathcal{T}_{\bar{I}\bar{J}}$, which is power conjugate to the plastic velocity gradient ${L^{\mathrm{p}}}_{\bar{J}\bar{I}} = {\dot{F}^{\mathrm{p}}}_{\bar{J}K}{(F^{\mathrm{p}})^{-1}}_{K\bar{I}}$, is defined exclusively in the intermediate configuration as

$$\mathcal{T}_{\bar{I}\bar{J}} = J\,{(F^{\mathrm{e}})^{-1}}_{\bar{I}i}\, t_{ij}\; {F^{\mathrm{e}}}_{j\bar{J}}\,. \tag{56}$$

Lastly, the Biot couple stress tensor M_{IJ}, power conjugate to ${\dot{\Gamma}^{\mathrm{e}}}_{JI}$ and ${\dot{\Gamma}^{\mathrm{p}}}_{JI}$, is introduced as

$$M_{IJ} = J\, m_{ij}\, {F^{-1}}_{Ii}\, \chi_{jJ}\,. \tag{57}$$

Following the derivations in [60], the Coleman-Noll procedure [13], requiring that non-negative dissipation must be fulfilled for arbitrary, independent rate processes, yields the the constitutive relations

$$T_{\bar{I}J} = \rho_0 \frac{\partial \Psi^{\mathrm{e}}}{\partial {\mathfrak{C}^{\mathrm{e}}}_{\bar{I}J}}\,, \quad M_{IJ} = \rho_0 \frac{\partial \Psi^{\mathrm{e}}}{\partial {\Gamma^{\mathrm{e}}}_{JI}}\,. \tag{58}$$

For the elastic constitutive relations, the potential function

$$\begin{aligned}\rho_0 \Psi^{\mathrm{e}}({\mathfrak{C}^{\mathrm{e}}}_{\bar{I}J}, {\Gamma^{\mathrm{e}}}_{JI}, \omega) = {} & g(J^{\mathrm{e}}) + (1-\omega)\,\frac{1}{2}\,\Big((G + G_{\mathrm{c}})\,\Big((J^{\mathrm{e}})^{-\frac{2}{3}}\, {\mathfrak{C}^{\mathrm{e}}}_{\bar{I}J}\, {\mathfrak{C}^{\mathrm{e}}}_{\bar{I}J} - 3 \Big) - G_{\mathrm{c}}\, \Big((J^{\mathrm{e}})^{-\frac{2}{3}}\, {\mathfrak{C}^{\mathrm{e}}}_{\bar{I}J}\, {\mathfrak{C}^{\mathrm{e}}}_{J\bar{I}} - 3 \Big) \Big) \\ & + (1-\omega)\,\frac{1}{2}\,\Big((\hat{\gamma} + \hat{\beta})\, {\Gamma^{\mathrm{e}}}_{JI}\, {\Gamma^{\mathrm{e}}}_{JI} + (\hat{\gamma} - \hat{\beta})\, {\Gamma^{\mathrm{e}}}_{JI}\, {\Gamma^{\mathrm{e}}}_{IJ} + \hat{\alpha}\, {\Gamma^{\mathrm{e}}}_{II} {\Gamma^{\mathrm{e}}}_{JJ} \Big)\,,\end{aligned} \tag{59}$$

is used, with J^{e} denoting the determinant of ${\mathfrak{C}^{\mathrm{e}}}_{\bar{I}J}$, and

$$g(J^{\mathrm{e}}) = \frac{K}{8}\left(J^{\mathrm{e}} - \frac{1}{J^{\mathrm{e}}} \right)^2\,. \tag{60}$$

The six elastic constants are the shear modulus G, the bulk modulus K, the coupling modulus G_{c}, and the three micropolar elastic constants $\hat{\alpha}$, $\hat{\beta}$ and $\hat{\gamma}$. The latter are commonly expressed using the polar ratio and the characteristic lengths in bending and torsion, i.e.,

$$\psi = \frac{2\hat{\gamma}}{2\hat{\gamma} + \hat{\alpha}}\,, \quad l_{\mathrm{b}} = \sqrt{\frac{\hat{\gamma} + \hat{\beta}}{4G}}\,, \quad l_{\mathrm{t}} = \sqrt{\frac{\hat{\gamma}}{G}}\,. \tag{61}$$

Following the principle of bounded stiffness [55] leads to the choice

$$\psi = \frac{3}{2} \quad \text{and} \quad l_{\mathrm{t}} = 2\, l_{\mathrm{b}}\,. \tag{62}$$

Accordingly, only the length scale parameter l_{b} and the coupling modulus G_{c} remain as independent elastic parameters, together with the classical constants G and K.

The evolution of the plastic deformation tensor ${F^{\mathrm{p}}}_{\bar{I}I}$ and the plastic wryness ${\Gamma^{\mathrm{p}}}_{JI}$, as well as an assumed internal state variable α_{p} accounting for the hardening state, are described by means of a yield condition, a flow rule, and a hardening rule. For the combined damage-plasticity approach, plasticity is formulated in the effective stress space

$$\bar{T}_{\bar{I}J} = \rho_0 \left.\frac{\partial \Psi^{\mathrm{e}}}{\partial {\mathfrak{C}^{\mathrm{e}}}_{\bar{I}J}}\right|_{\omega=0} , \quad \bar{M}_{IJ} = \rho_0 \left.\frac{\partial \Psi^{\mathrm{e}}}{\partial {\Gamma^{\mathrm{e}}}_{JI}}\right|_{\omega=0} , \tag{63}$$

interpreted as forces per intact area of the material.

A single, combined yield function exploiting the concept of generalized stress invariants [54, 76], computed from both the effective Mandel and couple stress tensors, $\bar{\mathcal{T}}_{\bar{I}\bar{J}}$ and $\bar{M}_{IJ}$, is used. Following the discussion in [58, 57], those generalized invariants $\hat{\bar{I}}_1$ and $\hat{\bar{J}}_2$ are computed as

$$\hat{\bar{I}}_1 = \bar{\mathcal{T}}_{\bar{I}\bar{I}} , \tag{64}$$

and

$$\hat{\bar{J}}_2 = \frac{1}{2} \bar{\mathcal{S}}_{\bar{I}\bar{J}} \, \bar{\mathcal{S}}_{\bar{I}\bar{J}} + \frac{1}{(l_{\mathrm{J2}})^2} \left(\frac{1}{2} \bar{M}_{IJ} \, \bar{M}_{IJ} \right) , \tag{65}$$

from the deviatoric part of the effective Mandel stress tensor

$$\bar{\mathcal{S}}_{\bar{I}\bar{J}} = \bar{\mathcal{T}}_{\bar{I}\bar{J}} - \frac{1}{3} \delta_{\bar{I}\bar{J}} \, \hat{\bar{I}}_1 . \tag{66}$$

Therein, the length scale parameter l_{J2} is a material parameter specific to the microstructure of the material.

The single combined yield function is expressed as

$$f_{\mathrm{p}}(\bar{\mathcal{T}}_{\bar{I}\bar{J}} , \bar{M}_{IJ} , \bar{\beta}_{\mathrm{p}}) = \sqrt{\frac{3}{2}} \, \hat{\bar{\rho}} + \sqrt{3} \left(m_\phi \, \hat{\bar{\mathcal{T}}}_{\mathrm{m}} - \beta_0 \right) - \bar{\beta}_{\mathrm{p}} , \tag{67}$$

with

$$\hat{\bar{\mathcal{T}}}_{\mathrm{m}} = \frac{1}{3} \, \hat{\bar{I}}_1 , \quad \hat{\bar{\rho}} = \sqrt{2 \, \hat{\bar{J}}_2} , \tag{68}$$

with m_ϕ denoting the friction parameter, β_0 denoting the cohesion strength parameter, and $\beta_{\mathrm{p}} = (1-\omega) \, \bar{\beta}_{\mathrm{p}}$ as the nominal scalar stress-like hardening parameter. The latter is related to the conjugate equivalent plastic deformation measure α_{p} as

$$\beta_{\mathrm{p}} = (1-\omega) \rho_0 \frac{\partial \Psi^{\mathrm{h}}}{\partial \alpha_{\mathrm{p}}}, \quad \text{with} \quad \rho_0 \, \Psi^{\mathrm{h}} = h_\Delta \left(\alpha_{\mathrm{p}} + \frac{\exp(-\alpha_{\mathrm{p}} \, h_{\mathrm{exp}}) - 1}{h_{\mathrm{exp}}} \right) , \tag{69}$$

where h_Δ and h_{exp} are hardening material parameters.

The evolution of ${F^{\mathrm{p}}}_{\bar{I}I}$, ${\Gamma^{\mathrm{p}}}_{JI}$ and α_{p} follows from the flow rules

$${L^{\mathrm{p}}}_{\bar{J}\bar{I}} = \dot{\lambda} \, \frac{\partial g_{\mathrm{p}}(\bar{\mathcal{T}}_{\bar{I}\bar{J}} , \bar{M}_{IJ})}{\partial \bar{\mathcal{T}}_{\bar{I}\bar{J}}} , \quad {\dot{\Gamma}^{\mathrm{p}}}{}_{JI} = \dot{\lambda} \, \frac{\partial g_{\mathrm{p}}(\bar{\mathcal{T}}_{\bar{I}\bar{J}} , \bar{M}_{IJ})}{\partial \bar{M}_{IJ}} , \quad \dot{\alpha}_{\mathrm{p}} = -\dot{\lambda} \, \frac{\partial f_{\mathrm{p}}(\bar{\mathcal{T}}_{\bar{I}\bar{J}} , \bar{M}_{IJ} , \bar{\beta}_{\mathrm{p}})}{\partial \bar{\beta}_{\mathrm{p}}} , \tag{70}$$

with $\dot{\lambda}$ denoting the plasticity consistency parameter, and with the non-associated plastic potential function $g_{\mathrm{p}}(\bar{\mathcal{T}}_{\bar{I}\bar{J}} , \bar{M}_{IJ} , \beta_\psi)$ defined as

$$g_{\mathrm{p}}(\bar{\mathcal{T}}_{\bar{I}\bar{J}} , \bar{M}_{IJ}) = \sqrt{\frac{3}{2}} \, \hat{\bar{\rho}} + \sqrt{3} \left(m_\psi \, \hat{\bar{\mathcal{T}}}_{\mathrm{m}} \, \frac{\beta_\psi}{(1-\omega)} \right) . \tag{71}$$

Therein, m_ψ is the dilation parameter, and β_ψ is a dimensionless parameter for modeling decreasing dilatant

Table 1: Material parameters for Gosford sandstone used in the numerical examples.

E (GPa)	ν (-)	G_c/G (-)	l_b (mm)	l_d (mm)	l_{J2} (mm)	c (MPa)	ϕ (°)	ψ (°)	A (-)	h_Δ (MPa)	h_{exp} (-)	h_d (-)	ε_f (-)
13	0.35	1	1	1	1	8	30	20	1	11	1400	1	0.11

behavior with evolving plastic deformations as

$$\beta_\psi = 1 - \exp(-\alpha_p\, h_d)\,, \tag{72}$$

utilizing the material parameter h_d.

Parameters β_0, m_ϕ and m_ψ in equations (67) and (71) are computed as

$$\beta_0 = \frac{6\,c\,\cos(\phi)}{\sqrt{3}(3 + A\,\sin\phi)}\,, \quad m_\phi = \frac{6\,\sin(\phi)}{\sqrt{3}(3 + A\,\sin\phi)}\,, \quad m_\psi = \frac{6\,\sin(\psi)}{\sqrt{3}(3 + A\,\sin\psi)}\,, \tag{73}$$

in which c denotes the cohesion stress like material parameter, ϕ the friction angle, ψ the angle of dilation and $-1 \leq A \leq 1$ a fitting parameter for adjusting the Drucker-Prager yield surface for in- ($A = 1$) or circumscribing ($A = -1$) the Mohr-Coulomb yield surface.

For describing the evolution of damage, the exponential softening law

$$\omega = 1 - \exp\left(-\frac{\tilde{\alpha}}{\varepsilon_f}\right), \tag{74}$$

is used, with ε_f as the softening modulus, and with $\tilde{\alpha}$ denoting the independent field describing the integrity of the material in Eq. (8).

The local damage driving variable α_d is related to the accumulation of plastic dilation as

$$\dot{\alpha}_d = \frac{\mathrm{D}}{\mathrm{D}t}\left(\log\left(\det F^{p}{}_{\bar{I}I}\right)\right)\,. \tag{75}$$

This way, a monotonic growth of the damage parameter ω is ensured. The employed material parameters, which have been calibrated in [60] based on the experimental results on specimen `RA0636` by [63], are summarized in Table 1. At material point level, the constitutive relations are implemented by means of a stress update algorithm, computing in the time interval $[t_{(old)}, t = t_{(old)} + \Delta t]$ for the given total deformation state F_{iI}, w_i and $w_{i,J}$ and the known state of the material at time $t_{(old)}$ (i) the updated Kirchhoff stress $\tau_{ij}(t)$, (ii) the updated Kirchhoff couple stress $\mu_{ij}(t)$, (iii) the updated damage driving variable $\alpha_d(t)$, and (iv) the updated hardening variable $\alpha_p(t)$. Additionally, (v) the algorithmic tangents of $\tau_{ij}(t)$, $\mu_{ij}(t)$, and $\alpha_d(t)$ with respect to the deformation tensors are computed, which are required for solving the global system of equations using the Newton scheme. The employed stress update algorithm is briefly outlined in Algorithm 2. For detailed explanations of the implementation, especially the finite strain return mapping algorithm of the plasticity part, we refer to [60, 23].

3.2. Plane strain compression tests on Gosford sandstone

As a first numerical example, we consider one of the biaxial compression tests under plane strain conditions on Gosford sandstone carried out by Ord et al. [63]. This test has already been investigated by the authors in [60] in the context of the finite element method. In the following, the finite element results are compared to the results achieved using the present gmp-iMPM. In [63], prismatic sandstone specimens (40 mm × 80 mm × 80 mm) were tested under plane strain conditions at constant lateral confining pressures ranging from 0 MPa to 20 MPa. In the numerical model, possible relative displacements between the loading plates and bottom and top surfaces

Algorithm 2 GOSFORD SANDSTONE MODEL – STRESS UPDATE

Input: F_{iI}, w_i, $w_{i,I}$, $\tilde{\alpha}$, $(F^{\mathrm{p}}{}_{\bar{I}I})_{(\mathrm{old})}$, $(\Gamma^{\mathrm{p}}{}_{JI})_{(\mathrm{old})}$, $(\alpha_{\mathrm{p}})_{(\mathrm{old})}$, $(\alpha_{\mathrm{d}})_{(\mathrm{old})}$

Output: τ_{ij}, μ_{ij}, α_{d} and tangents, $F^{\mathrm{p}}{}_{\bar{I}I}$, $\Gamma^{\mathrm{p}}{}_{JI}$, α_{p},

χ_{iI}, $\chi_{iI,J}$ $\leftarrow$ ROTATION INTEGRATOR $(w_i,\ w_{i,I})$ ▷ Update micro rotation tensor and its gradient using (4)

$\mathfrak{C}_{IJ}$, Γ_{JI} $\leftarrow$ F_{iI}, χ_{iJ}, $\chi_{iL,I}$ ▷ Compute deformation measures in (46) and (47)

procedure PLASTICITY PART

  $\mathfrak{C}^{\mathrm{e,tr}}{}_{\bar{I}J}$, $\Gamma^{\mathrm{e,tr}}{}_{JI}$ $\leftarrow$ $\mathfrak{C}_{IJ}$, Γ_{JI}, $(F^{\mathrm{p}}{}_{\bar{I}I})_{(\mathrm{old})}$, $(\Gamma^{\mathrm{p}}{}_{JI})_{(\mathrm{old})}$ ▷ Assume trial elastic state using (50) and (51)

  $\bar{\mathcal{T}}_{\bar{I}\bar{J}}$, $\bar{M}_{IJ}$, $\bar{\beta}_{\mathrm{p}}$ $\leftarrow$ $\mathfrak{C}^{\mathrm{e,tr}}{}_{\bar{I}J}$, $\Gamma^{\mathrm{e,tr}}{}_{JI}$, $(\alpha_{\mathrm{p}})_{(\mathrm{old})}$, $\omega = 0$ ▷ Compute effective trial state using (63), (56) and (69)

  $f_{\mathrm{p}}(\bar{\mathcal{T}}_{\bar{I}\bar{J}}, \bar{M}_{IJ}, \bar{\beta}_{\mathrm{p}})$ $\leftarrow$ $\bar{\mathcal{T}}_{\bar{I}\bar{J}}$, $\bar{M}_{IJ}$, $\bar{\beta}_{\mathrm{p}}$ ▷ Evaluate the yield function (67)

  if $f_{\mathrm{p}}(\bar{\mathcal{T}}_{\bar{I}\bar{J}}, \bar{M}_{IJ}, \bar{\beta}_{\mathrm{p}}) > 0$ **then**

    $\mathfrak{C}^{\mathrm{e}}{}_{\bar{I}J}$, $\Gamma^{\mathrm{e}}{}_{JI}$, α_{p} $\leftarrow$ RETURN MAPPING $((F^{\mathrm{p}}{}_{\bar{I}I})_{(\mathrm{old})}, (\Gamma^{\mathrm{p}}{}_{JI})_{(\mathrm{old})}, (\alpha_{\mathrm{p}})_{(\mathrm{old})}, \mathfrak{C}_{IJ}, \Gamma_{JI})$

    ▷ Numerical integration of (70)

    $F^{\mathrm{p}}{}_{\bar{I}I}$, $\Gamma^{\mathrm{p}}{}_{JI}$ $\leftarrow$ $\mathfrak{C}_{IJ}$, Γ_{JI}, , $\mathfrak{C}^{\mathrm{e}}{}_{\bar{I}J}$, $\Gamma^{\mathrm{e}}{}_{JI}$, ▷ Update plastic state using (50) and (51)

    α_{d} $\leftarrow$ α_{p}, $(\alpha_{\mathrm{p}})_{(\mathrm{old})}$, $\bar{\mathcal{T}}_{\bar{I}\bar{J}}$ ▷ Compute local damage driving parameter in (75)

  else

    $F^{\mathrm{p}}{}_{\bar{I}I}$, $\Gamma^{\mathrm{p}}{}_{JI}$, α_{p} $\leftarrow$ $(F^{\mathrm{p}}{}_{\bar{I}I})_{(\mathrm{old})}$, $(\Gamma^{\mathrm{p}}{}_{JI})_{(\mathrm{old})}$, $(\alpha_{\mathrm{p}})_{(\mathrm{old})}$ ▷ No plastic response

    α_{d} $\leftarrow$ $(\alpha_{\mathrm{d}})_{(\mathrm{old})}$ ▷ No change in local damage driving force

  end if

end procedure

procedure DAMAGE PART

  ω $\leftarrow$ $\tilde{\alpha}$ ▷ Compute updated damage parameter in (74)

end procedure

$T_{\bar{I}J}$, M_{IJ} $\leftarrow$ $\mathfrak{C}^{\mathrm{e}}{}_{\bar{I}J}$, $\Gamma^{\mathrm{e}}{}_{JI}$, ω ▷ Compute nominal Biot stress measures using (58)

τ_{ij}, μ_{ij} $\leftarrow$ $T_{\bar{I}J}$, M_{IJ} ▷ Push forward to nominal Kirchhoff stress measures

are neglected, resulting in fixed boundary conditions at the bottom and a rigid body constraint at the top surface. Additionally, a relative rotation between the bottom and top surfaces is not permitted. Furthermore, for triggering the shear band direction with an imperfection, a small lateral force of 10 N is applied at the top right corner of the specimen. In the model using the gmp-iMPM, only the fixed boundary condition at the bottom surface is applied directly on the background mesh, whereas the rigid body constraint and the displacement at the top surface are weakly imposed as described in Section 2.5. The simulation of the plane strain compression tests is performed in two sequential steps: First, the confining pressure is applied while any vertical displacement is blocked at the top surface. Subsequently, an adaptive time incrementation scheme is employed for applying the displacement at the top surface.

In the following, for comparing the present gmp-iMPM to the FEM, the test with 20 MPa confining pressure is investigated. The test setup, including the boundary conditions together with the respective discretization using the MPM approach, is illustrated in Fig. 4. For the FEM, 60×120 elements with second order Lagrangian shape functions and a reduced Gaussian quadrature rule are employed, c.f. [60] for details on the discretization and boundary conditions using the FEM.

For discretizing the background domain with dimensions of 60 mm × 80 mm, two resolutions with 30×40 and 60×80 cells are considered. Moreover, for all background meshes B-splines of order 1, 2, and 3 are investigated. Similarly, for all background meshes, different discretizations of the specimens are investigated, consisting of 80×160, 120×240 and 160×320 material points.

Fig. 5 illustrates the evolution of the displacement field in the specimen during the simulation. It can be seen that during the test, a diagonal shear band emerges, resulting in localization of the deformations. The respective load-displacement curves are shown in Fig. 6, together with the reference FEM solution from [60]. It can be seen that the coarser background discretization is insufficient for obtaining an accurate agreement with the FEM solution in the post peak regime, irrespective of the B-spline order and the number of material points. By contrast, for the fine background resolution, very good agreement is obtained for second and third order B-splines, irrespective of the number of material points. For the first order B-splines, which are equal to classical linear Lagrangian shape functions, not only a ductile post peak response is obtained, but also oscillations are observed. The first issue, i.e., the overly ductile response, is attributed to locking behavior in shear deformations, similar to the well known issues in the context of the FEM. In particular, the complex kinematics in case of shear band dominated failure cannot be represented properly by such low order cells. The second issue, i.e., oscillations in the load-displacement curves, are a result of the well known cell crossing problems, which are completely remedied by higher order B-splines providing higher order continuity for derivatives.

Fig. 7 illustrates a detailed view of the shear band at a later stage of the simulation for both the MPM and the FEM. It can be seen clearly that for large localized deformations, for the FEM mesh distortion becomes excessive, resulting in severely warped and entangled elements, which ultimately terminates the simulation.

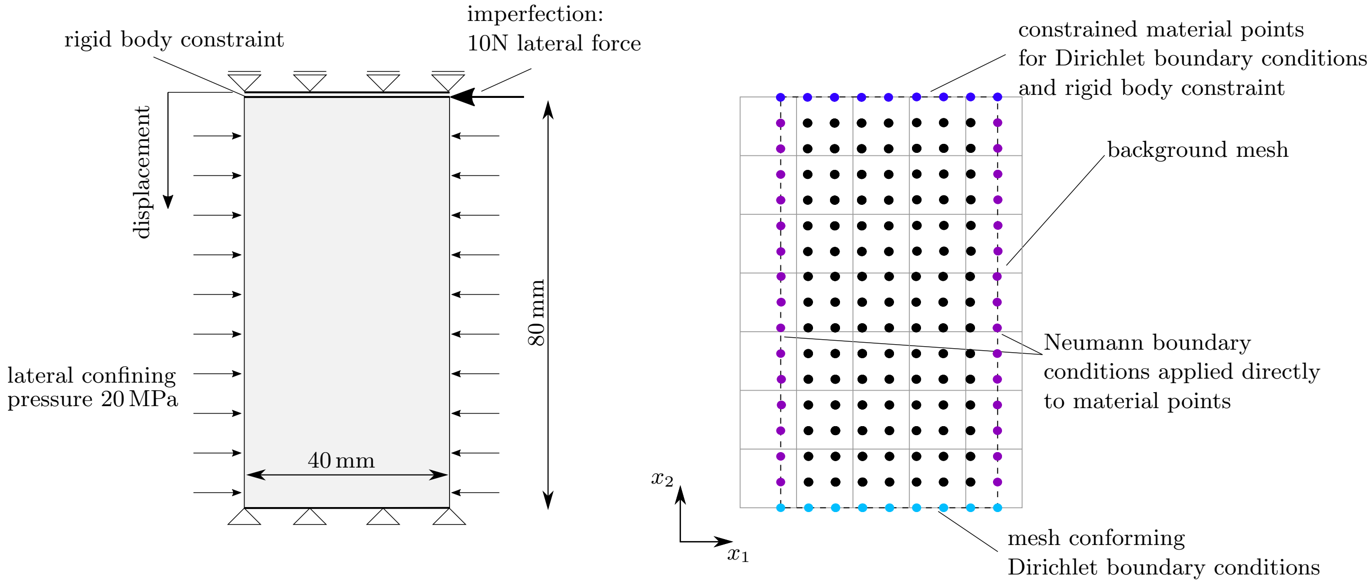

Figure 4: Geometry and boundary conditions (left) and illustration of the respective MPM discretization for the 2D plane strain compression test on Gosford sandstone.

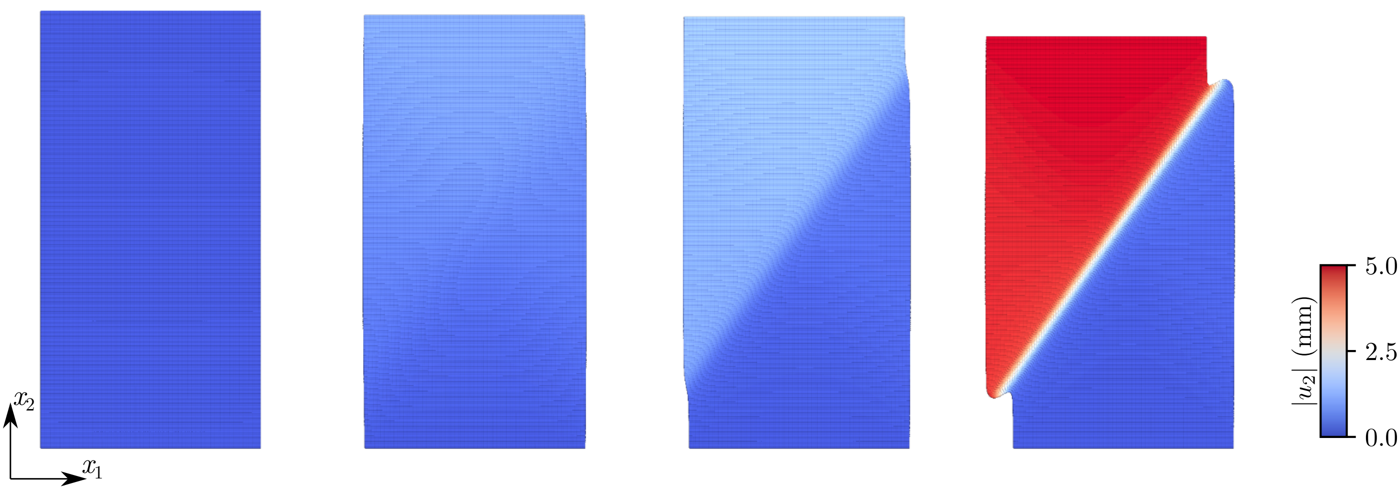

Figure 5: Evolution of the magnitude of the vertical displacement in the prismatic specimen for different stages of the simulation, indicating the formation of a diagonal shear band with strongly localized inelastic deformations. The simulation is based on the 60×80 third order B-spline background cells with 160 × 320 material points.

3.3. Triaxial extension tests on Gosford sandstone

In order to further investigate the capabilities of the gmp-iMPM, we consider a triaxial extension test on a cylindrical specimen with a height to diameter ratio of one employing the same constitutive model. The respective test setup and discretization using the gmp-iMPM is illustrated in Fig. 8. In order to reduce the

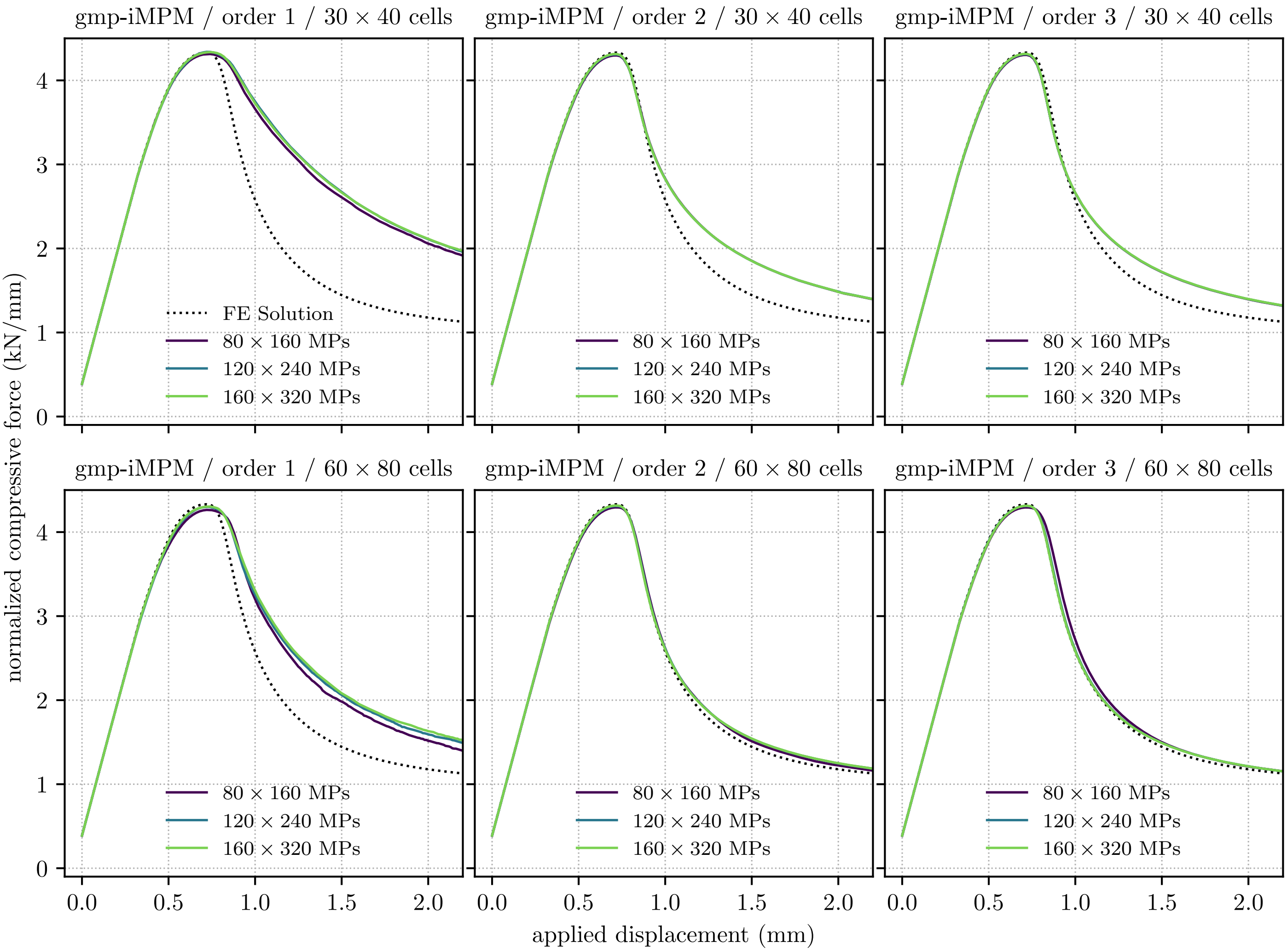

Figure 6: Load–displacement curves for the plane strain compression tests using the FEM with second order Lagrangian shape functions and a reduced Gaussian quadrature rule, and the MPM with B-splines of order 1, 2, and 3. For the MPM, three different material point discretization are employed.

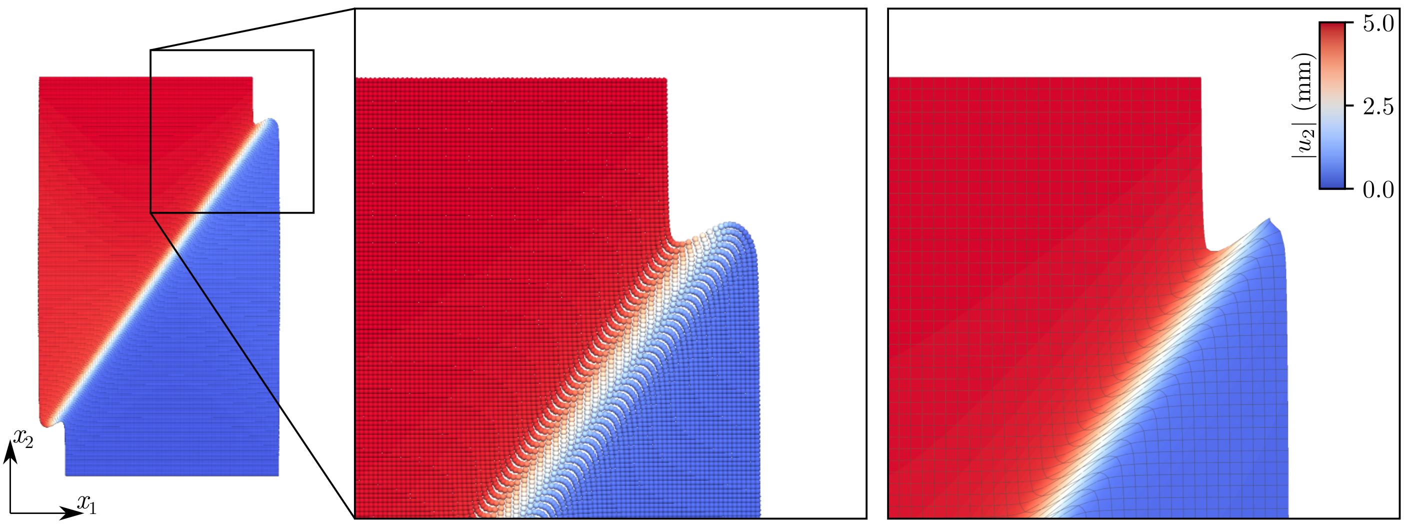

Figure 7: Contour plot of the magnitude of the vertical displacement in the specimen at an applied displacement of 5 mm, and detail view of the shear band obtained using the MPM with 40×80 third order B-spline cells with 160×320 material points (left), and the FEM (right). For the FEM, severe distortion of the mesh occurs, resulting in collapsing elements.

computational effort, the symmetry is exploited in the simulations. Apart from the symmetry conditions, the boundary conditions assumed in the triaxial extension test are quite similar to the plane strain compression test. Accordingly, the top and bottom surfaces are constrained, and a relative rotation between them is not possible. Furthermore, again for triggering the direction of the emerging shear band using an imperfection, a small lateral force of 10 N is applied in the x_3 direction at the top surface.

Similar to the previous 2D plane strain model, the fixed boundary condition at the bottom surface is applied, conforming with the background mesh, whereas the constraint and the Dirichlet boundary condition at the top surface are weakly imposed. Additionally, the boundary condition following from the symmetry exploitation is applied in a mesh conforming way. Furthermore, the simulation is carried out in accordance to the plane strain compression test, i.e., applying the confining pressure of 20 MPa while top and bottom surfaces are fixed, and subsequently increasing the displacement of the top surface.

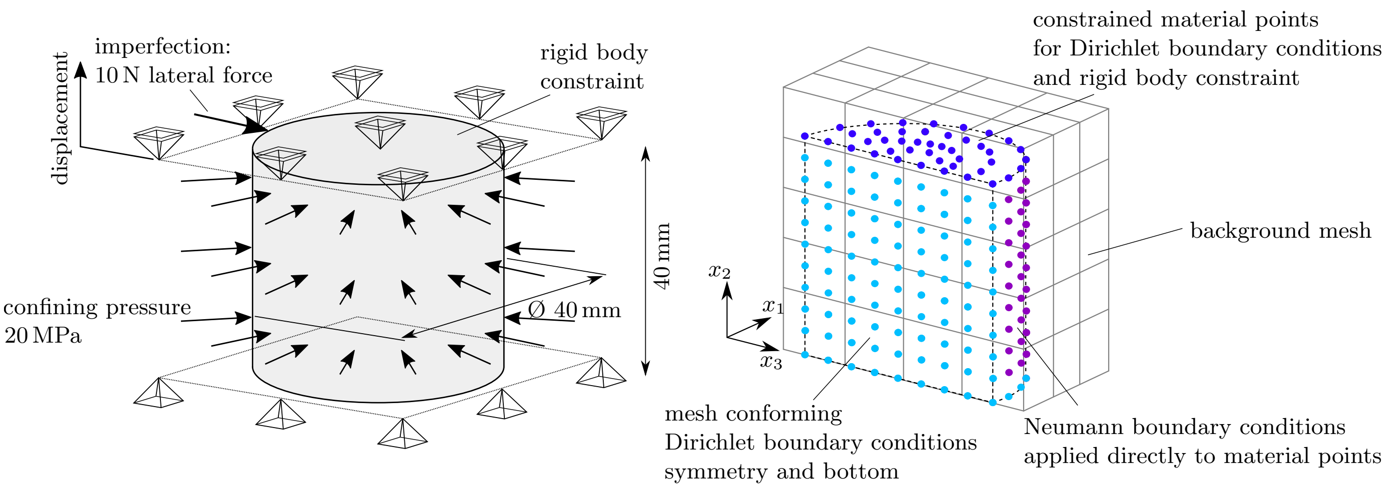

Figure 8: Geometry and boundary conditions (left) and illustration of the respective MPM discretization (right) for the triaxial extension test.

As concluded from the previous example, second order B-splines are sufficient for overcoming numerical locking upon inelastic plastic flow, and provide good accuracy. Moreover, compared to third order B-splines, they are characterized by a drastically lower computational effort. This is of particular great importance for 3D simulations. In 3D, third order B-splines result in a large bandwidth of the sparsity pattern of the global system matrix, and for the present gradient-enhanced micropolar continuum with seven degrees of freedom per node, each cell stiffness matrix has $(4 \times 4 \times 4 \times 7)^2 = 448^2$ entries, compared to the $(3 \times 3 \times 3 \times 7)^2 = 189^2$ entries in case of second order B-splines. For these reasons, we restrict the discussion to second order B-splines.

For the FEM model, a mesh consisting of 7479 second order Lagrangian elements with an average element size of 1.5 mm and reduced Gaussian quadrature is used, yielding a global system of equations with the size of 235 368. For the gmp-iMPM model with second order B-splines, background mesh resolutions consisting of 30×30×30 cells, 40×40×40 cells, and 50×50×50 cells are utilized, resulting in global systems of equations with approximate sizes of 60 000 (30×30×30 cells), 130 000 (40×40×40 cells), and 240 000 (50×50×50 cells). Similar to the previous example, for the gmp-iMPM model different material point discretizations of the cylinder are investigated, ranging from $80 \times 2531 = 202\,480$ to $140 \times 7730 = 1\,082\,200$ material points. For comparison, the FEM model has a total of 59 832 quadrature points.

Fig. 9 illustrates the evolution of the displacement field in the cylindrical specimen at different stages of the test. During the test, after attaining the peak load, deformations in the center of the specimen are increasing and subsequently localize, resulting in the formation of a single shear band spanning diagonally across the specimen.

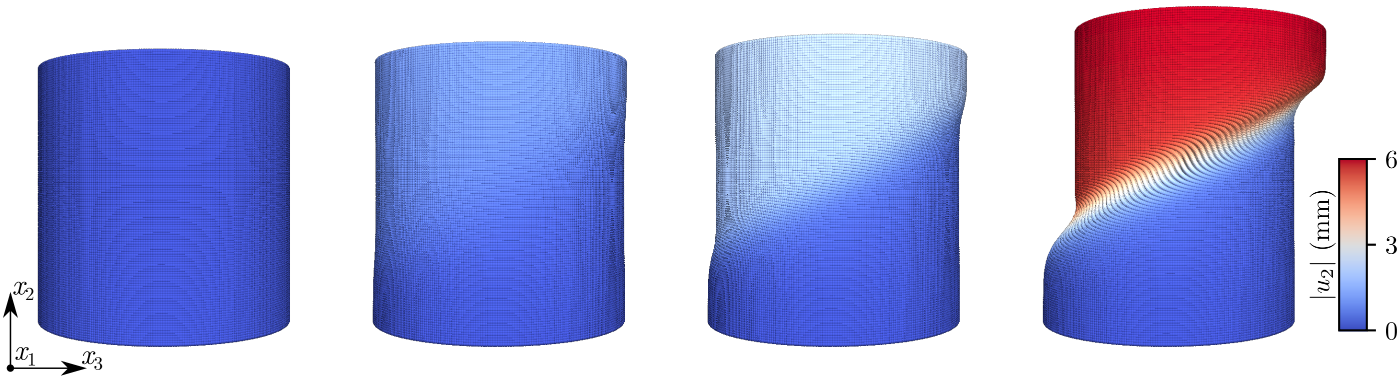

Figure 9: Evolution of the magnitude of the vertical displacement in the cylindrical specimen for different stages of the simulation, indicating the formation of a diagonal shear band with strongly localized inelastic deformations. The simulation is based on 40×40×40 second order B-spline background cells with 120 × 5684 material points.

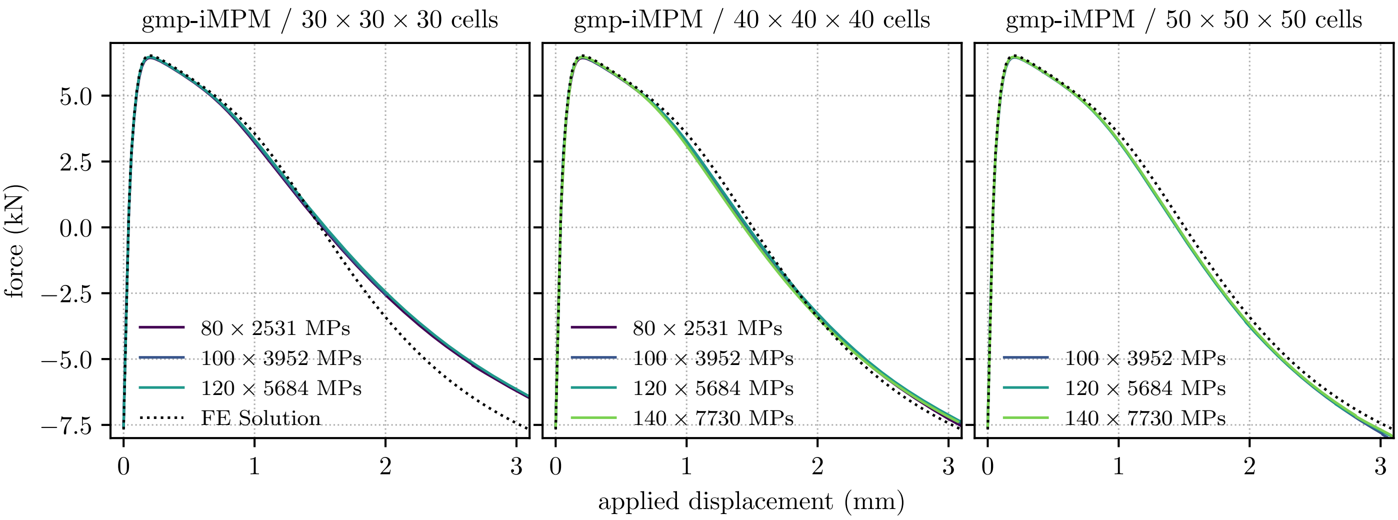

Figure 10: Load–displacement curves for the triaxial extension tests on cylindrical specimens using the FEM with second order Lagrangian shape functions and a reduced Gaussian quadrature rule, and the MPM with B-splines of order 2. For the MPM, three different background mesh resolutions (30×30×30 (left), 40×40×40 (center), and 50×50×50 (right)), and different refinements of the material point discretization are investigated.

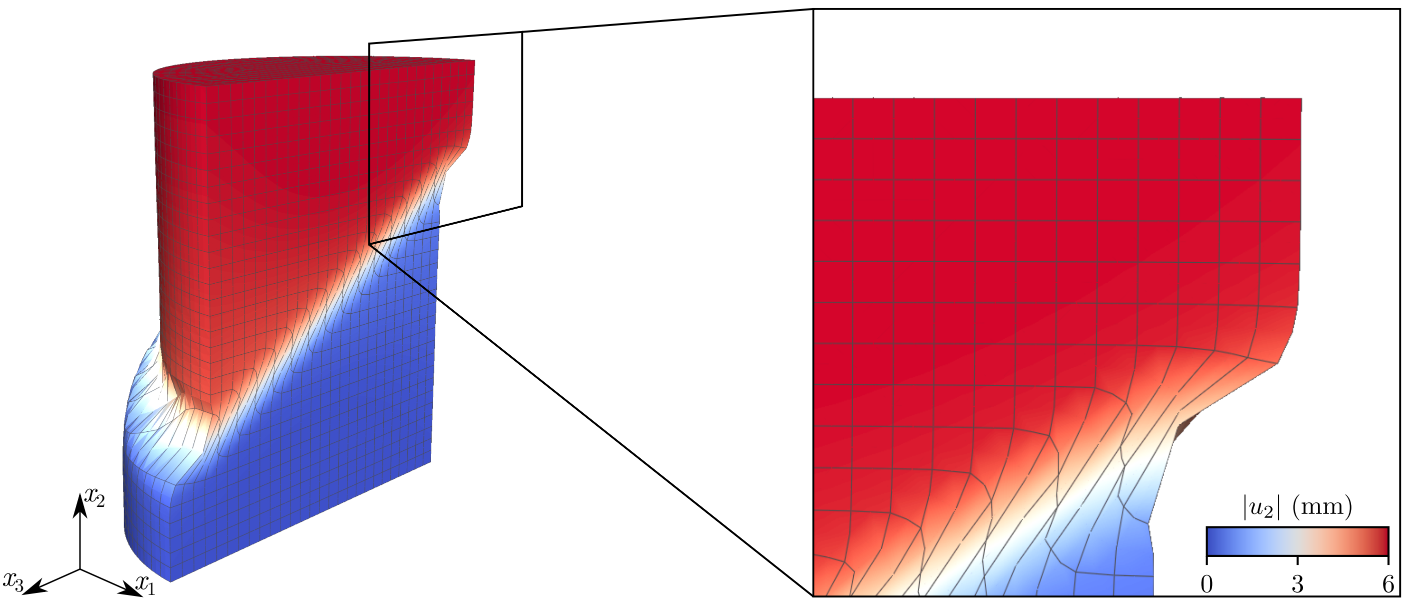

Figure 11: Contour plot of the magnitude of the vertical displacement using the FEM with second order Lagrangian elements and reduced Gaussian quadrature at an applied displacement of 6 mm. Similar to the plane strain compression test, severe mesh distortion occurs in the region of the shear band.

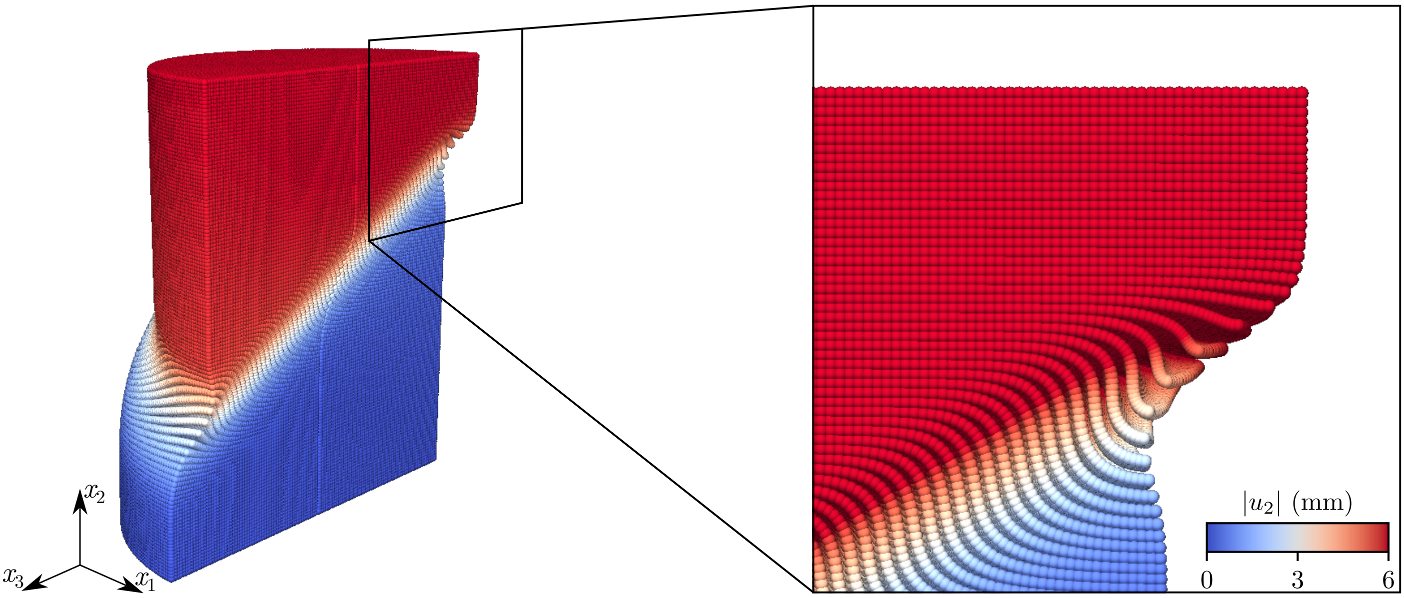

Figure 12: Contour plot of the magnitude of the vertical displacement at an applied displacement of 6 mm, using the MPM (B-spline order 2, 120×5684 material points, 40×40×40 background cells).

The obtained load-displacement curves are shown in Fig. 10. Comparing the FEM and gmp-iMPM results, it can be seen that the 30×30×30 cells resolution is too coarse, resulting in a slight discrepancy between the gmp-iMPM and the reference FEM solution in the far post peak regime. However, both finer background mesh resolutions are in very good agreement with the FEM results.

For the simulation using the FEM, similar to the 2D example the emerging shear band results in severe mesh distortion, see Fig. 11. By comparison, an expected displacement field is obtained using the gmp-iMPM as shown in Fig. 12, confirming the suitability of the gmp-iMPM for representing large localized deformations.

3.4. Remarks on computational effort

The MPM is commonly attributed with a higher computational effort compared to the FEM due to additional required steps in the computational procedure. While for the present examples it was found that the overall runtimes were longer, it was also found that similar to the FEM the major part of the computational effort is spent on solving the global system of equations. For instance, Table 2 summarizes the computational effort of individual tasks for the largest investigated MPM simulation with 50×50×50 cells and 1 082 200 material points. In particular, it can be seen that MPM specific tasks such as the tracing of the material points using the k-d tree algorithm, and the interpolation of the solution from the background mesh to the material points, i.e., the convective phase, are barely noticeable in the overall computational effort. Moreover, despite the considerably larger number of material points compared to the FEM, the cost of the stress update and the computation of the cell residuals and stiffness matrices are moderate and amount only to 6 % of the total computational effort.

However, compared to the FEM an additional effort results from the fact that the set of active cells changes during the simulation, and accordingly the global sparsity pattern needs to be reanalyzed several times during the simulation, leading to a higher cumulative effort than the evaluation of cell residuals and tangents, and the stress update combined. Furthermore, for all the investigated examples, in general, more time steps were required compared to the FEM, further increasing the simulation times.

4. Summary and Conclusions

An extended formulation of the material point method for the gradient-enhanced micropolar continuum was proposed, aiming at the analysis of strongly localized inelastic deformations resulting from shear band

task	remark	relative effort
tracing of material points in cells using a k-d tree[1] (Section 2.7)		$< 1\,\%$
stress update (Algorithm 2, cf. also [23])	in parallel	$2\,\%$
2nd order B-spline cells: internal kernels (25), (26), (27), and tangents	in parallel	$4\,\%$
rigid body constraint residual contributions	non optimized	$5\,\%$
analysis of the sparse matrix pattern from active cell connectivity[2]		$8\,\%$
assembly of the sparse matrix from cell contributions		$3\,\%$
linear solver (`Intel PARDISO`)	in parallel	$72\,\%$
interpolation of solution from nodes to material points[1]		$< 1\,\%$
remainder (e.g., data handling, boundary conditions, postprocessing, ...)		$5\,\%$
		$100\,\%$

Table 2: Distribution of the computational effort for the triaxial extension test with $50\times50\times50$ second order B-spline background mesh cells and 1 082 200 material points using 28 cores of two `Intel(R) Xeon(R) CPU E5-2690v4`.
[1]Tasks specific to the MPM compared to the FEM.
[2]This task is required and executed only if the set of active cells changes.

dominated failure of cohesive-frictional materials.

The proposed method, denoted as gmp-iMPM, was developed based on the recently proposed unified gradient-enhanced micropolar continuum, of which the prognosis capabilities were confirmed in previous studies using the FEM. For mitigating the well known issues such as locking behavior upon plastic flow or cell crossing errors, the method makes use of higher order B-spline based shape functions for the background mesh.

For assessing the gmp-iMPM, a numerical study was conducted, investigating shear band dominated failure of sandstone specimens in plane strain compression and triaxial extension. Reference simulations using the classical Lagrangian FEM revealed excessive mesh distortion, limiting the suitability in case of extreme deformations. It was confirmed that the gmp-iMPM is suitable for representing the arising excessive deformations. Furthermore, it was shown that second order B-splines are sufficient for overcoming the well known issues related to locking and cell crossing, and they represent a good compromise regarding computational efficiency.

By analyzing the distribution of the computational effort, it was highlighted that the major effort of the gmp-iMPM, similar to the FEM, is the solution of the global system of equations, whereas MPM specific tasks, such as the tracing of material points in the background mesh leveraging a simple yet effective k-d tree algorithm, or the convective phase for updating the position of the material points, are virtually negligible in terms of computational cost.

Final remarks concern a well known, fundamental issue of the standard MPM, which results from the fact that cell residual and stiffness are, in general, integrated non-optimally, with potential under-integration. Moreover, in certain cases, if the supports of cell shape functions are only partially covered by material points at the boundary of a body, an ill-conditioned or rank deficient global system of equations may be obtained. As a consequence, large jumps in the solution increments at the respective nodes of the background mesh may be obtained, leading to spuriously large deformation increments at certain material points at the boundary of a body. This issue is described and illustrated in [85], together with an extension of the B-spline MPM denoted as (Enhanced B-spline) EBS-MPM for mitigating such issues. Those issues have been observed also sporadically during the presented numerical study. In order to remedy such numerical stability issues, we are currently investigating the extension of the gmp-iMPM to stabilization concepts such as the EBS-MPM.

5. Acknowledgments

Financial support for this research was provided by the Austrian Science Fund (FWF) under Award Number 10.55776/PAT1342523 , and the Department of Energy, National Nuclear Security Administration, Predictive

Science Academic Alliance Program (PSAAP) under Award Number DE-NA0003962. This support is gratefully acknowledged.

References

[1] Aifantis, E. C. (1987). The physics of plastic deformation. *International Journal of Plasticity*, 3(3):211–247.

[2] Bardenhagen, S. and Kober, E. (2004). The Generalized Interpolation Material Point Method. *Computer Modeling in Engineering & Sciences*, 5(6):477–496.

[3] Bažant, Z. P. (1991). Why continuum damage is nonlocal: Micromechanics arguments. *Journal of Engineering Mechanics*, 117(5):1070–1087.

[4] Bažant, Z. P. and Planas, J. (2019). *Fracture and Size Effect in Concrete and Other Quasibrittle Materials*. Routledge, New York.

[5] Bažant, Z. P., Xi, Y., and Reid, S. G. (1991). Statistical size effect in quasi-brittle structures: I. Is Weibull theory applicable? *Journal of engineering Mechanics*, 117(11):2609–2622.

[6] Belytschko, T., Chen, J. S., and Hillman, M. (2023). *Meshfree and Particle Methods: Fundamentals and Applications*. John Wiley & Sons.

[7] Borja, R. I. (2013). *Plasticity*. Springer Berlin Heidelberg, Berlin, Heidelberg.

[8] Chambon, R., Caillerie, D., and El Hassan, N. (1998). One-dimensional localisation studied with a second grade model. *European Journal of Mechanics - A/Solids*, 17(4):637–656.

[9] Chandra, B., Singer, V., Teschemacher, T., Wüchner, R., and Larese, A. (2021). Nonconforming Dirichlet boundary conditions in implicit material point method by means of penalty augmentation. *Acta Geotechnica*, 16(8):2315–2335.

[10] Charlton, T. J., Coombs, W. M., and Augarde, C. E. (2017). iGIMP: An implicit generalised interpolation material point method for large deformations. *Computers & Structures*, 190:108–125.

[11] Chen, J.-S., Pan, C., Roque, C. M. O. L., and Wang, H.-P. (1998). A Lagrangian reproducing kernel particle method for metal forming analysis. *Computational Mechanics*, 22(3):289–307.

[12] Chen, J.-S., Pan, C., Wu, C.-T., and Liu, W. K. (1996). Reproducing Kernel Particle Methods for large deformation analysis of non-linear structures. *Computer Methods in Applied Mechanics and Engineering*, 139(1):195–227.

[13] Coleman, B. D. and Noll, W. (1963). The thermodynamics of elastic materials with heat conduction and viscosity. *Archive for Rational Mechanics and Analysis*, 13:167–178.

[14] Coombs, W., Augarde, C., Brennan, A., Brown, M., Charlton, T., Knappett, J., Ghaffari Motlagh, Y., and Wang, L. (2020). On Lagrangian mechanics and the implicit material point method for large deformation elasto-plasticity. *Computer Methods in Applied Mechanics and Engineering*, 358.

[15] Cosserat, E. and Cosserat, F. (1909). *Théorie Des Corps Déformables*. A. Hermann et fils.

[16] Cundall, P. A. (1971). A computer model for simulating progressive, large-scale movement in blocky rock system. In *Proceedings of the international symposium on rock mechanics*, volume 8, pages 129–136.

[17] Cundall, P. A. and Strack, O. D. (1979). A discrete numerical model for granular assemblies. *geotechnique*, 29(1):47–65.

[18] de Borst, R. (1988). Bifurcations in finite element models with a non-associated flow law. *International Journal for Numerical and Analytical Methods in Geomechanics*, 12(1):99–116.

[19] de Vaucorbeil, A., Nguyen, V. P., Sinaie, S., and Wu, J. Y. (2020). Material point method after 25 years: Theory, implementation, and applications. In *Advances in Applied Mechanics*, volume 53, pages 185–398. Elsevier.

[20] del Castillo, E. M., Fávero Neto, A. H., and Borja, R. I. (2021). Fault propagation and surface rupture in geologic materials with a meshfree continuum method. *Acta Geotechnica*, 16:2463–2486.

[21] del Castillo, E. M., Fávero Neto, A. H., and Borja, R. I. (2021). A continuum meshfree method for sandbox-style numerical modeling of accretionary and doubly vergent wedges. *Journal of Structural Geology*, 153:104466.

[22] Dummer, A., Mader, T., Neuner, M., and Schreter, M. (2021). Marmot library. https://github.com/MAteRialMOdelingToolbox/marmot.

[23] Dummer, A., Neuner, M., Gamnitzer, P., and Hofstetter, G. (2023). Robust and efficient implementation of finite strain generalized continuum models for fracture: Analytical, numerical, and automatic differentiation with hyper-dual numbers. *Preprint*.

[24] Dummer, A., Neuner, M., and Hofstetter, G. (2022). An extended gradient-enhanced damage-plasticity model for concrete considering nonlinear creep and failure due to creep. *International Journal of Solids and Structures*, 243:111541.

[25] Erdelj, S. G., Jelenić, G., and Ibrahimbegović, A. (2020). Geometrically non-linear 3D finite-element analysis of micropolar continuum. *International Journal of Solids and Structures*, 202:745–764.

[26] Eringen, A. C. (1968). Mechanics of Micromorphic Continua. In Kröner, E., editor, *Mechanics of Generalized Continua*, IUTAM Symposia, pages 18–35, Berlin, Heidelberg. Springer.

[27] Eringen, A. C. (1999). *Microcontinuum Field Theories*. Springer New York, New York, NY.

[28] Eringen, A. C. and Kafadar, C. B. (1976). Part I - Polar Field Theories. In Eringen, A. C., editor, *Continuum Physics*, pages 1–73. Academic Press.

[29] Eringen, A. C. and Suhubi, E. S. (1964). Nonlinear theory of simple micro-elastic solids—I. *International Journal of Engineering Science*, 2(2):189–203.

[30] Fávero Neto, A. H., Askarinejad, A., Springman, S. M., and Borja, R. I. (2020). Simulation of debris flow on an instrumented test slope using an updated Lagrangian continuum particle method. *Acta Geotechnica*, 15(10):2757–2777.

[31] Fávero Neto, A. H. and Borja, R. I. (2018). Continuum hydrodynamics of dry granular flows employing multiplicative elastoplasticity. *Acta Geotechnica*, 13(5):1027–1040.

[32] Forest, S. (2009). Micromorphic Approach for Gradient Elasticity, Viscoplasticity, and Damage. *Journal of Engineering Mechanics*, 135(3):117–131.

[33] Forest, S. and Sievert, R. (2003). Elastoviscoplastic constitutive frameworks for generalized continua. *Acta Mechanica*, 160(1-2):71–111.

[34] Forest, S. and Sievert, R. (2006). Nonlinear microstrain theories. *International Journal of Solids and Structures*, 43(24):7224–7245.

[35] Gray, J., Monaghan, J., and Swift, R. (2001). Sph elastic dynamics. *Computer Methods in Applied Mechanics and Engineering*, 190(49):6641–6662.

[36] Guilkey, J. E. and Weiss, J. A. (2003). Implicit time integration for the material point method: Quantitative and algorithmic comparisons with the finite element method. *International Journal for Numerical Methods in Engineering*, 57(9):1323–1338.

[37] Huang, T.-H., Wei, H., Chen, J.-S., and Hillman, M. C. (2020). RKPM2D: An open-source implementation of nodally integrated reproducing kernel particle method for solving partial differential equations. *Computational Particle Mechanics*, 7(2):393–433.

[38] Hughes, T. J. R., Cottrell, J. A., and Bazilevs, Y. (2005). Isogeometric analysis: CAD, finite elements, NURBS, exact geometry and mesh refinement. *Computer Methods in Applied Mechanics and Engineering*, 194(39):4135–4195.

[39] Iaconeta, I., Larese, A., Rossi, R., and Oñate, E. (2017). An Implicit Material Point Method Applied to Granular Flows. *Procedia Engineering*, 175:226–232.

[40] Iaconeta, I., Larese, A., Rossi, R., and Oñate, E. (2019). A stabilized mixed implicit Material Point Method for non-linear incompressible solid mechanics. *Computational Mechanics*, 63(6):1243–1260.

[41] Idelsohn, S., Oñate, E., and Pin, F. D. (2004). The particle finite element method: a powerful tool to solve incompressible flows with free-surfaces and breaking waves. *International Journal for Numerical Methods in Engineering*, 61(7):964–989.

[42] Iordache, M.-M. and Willam, K. (1998). Localized failure analysis in elastoplastic Cosserat continua. *Computer Methods in Applied Mechanics and Engineering*, 151(3-4):559–586.

[43] Jirásek, M. and Bažant, Z. P. (2002). *Inelastic Analysis of Structures*. John Wiley & Sons, Ltd.

[44] Kakouris, E. G. and Triantafyllou, S. P. (2017). Phase-field material point method for brittle fracture. *International Journal for Numerical Methods in Engineering*, 112(12):1750–1776.

[45] Kröner, E. (1959). Allgemeine Kontinuumstheorie der Versetzungen und Eigenspannungen. *Archive for Rational Mechanics and Analysis*, 4(1):273.

[46] Lee, E. H. and Liu, D. T. (1967). Finite-Strain Elastic—Plastic Theory with Application to Plane-Wave Analysis. *Journal of Applied Physics*, 38(1):19–27.

[47] Liang, Y., Benedek, T., Zhang, X., and Liu, Y. (2017). Material point method with enriched shape function for crack problems. *Computer Methods in Applied Mechanics and Engineering*, 322:541–562.

[48] Liu, W. K., Chen, Y., Jun, S., Chen, J. S., Belytschko, T., Pan, C., Uras, R. A., and Chang, C. T. (1996). Overview and applications of the reproducing Kernel Particle methods. *Archives of Computational Methods in Engineering*, 3(1):3–80.

[49] Ma, R. and Sun, W. (2022). A finite micro-rotation material point method for micropolar solid and fluid dynamics with three-dimensional evolving contacts and free surfaces. *Computer Methods in Applied Mechanics and Engineering*, 391:114540.

[50] Maugin, G. A. and Metrikine, A. V., editors (2010). *Mechanics of Generalized Continua: One Hundred Years After the Cosserats*, volume 21 of *Advances in Mechanics and Mathematics*. Springer New York, New York, NY.

[51] Mindlin, R. D. (1963). Microstructure in linear elasticity. Technical report, Columbia Univ New York Dept of Civil Engineering and Engineering Mechanics.

[52] Moresi, L., Dufour, F., and Mühlhaus, H. B. (2003). A Lagrangian integration point finite element method for large deformation modeling of viscoelastic geomaterials. *Journal of Computational Physics*, 184(2):476–497.

[53] Moutsanidis, G., Kamensky, D., Zhang, D. Z., Bazilevs, Y., and Long, C. C. (2019). Modeling strong discontinuities in the material point method using a single velocity field. *Computer Methods in Applied Mechanics and Engineering*, 345:584–601.

[54] Mühlhaus, H. B. and Vardoulakis, I. (1987). The thickness of shear bands in granular materials. *Géotechnique*, 37(3):271–283.

[55] Neff, P., Jeong, J., Münch, I., and Ramézani, H. (2010). Linear Cosserat elasticity, conformal curvature and bounded stiffness. In *Mechanics of Generalized Continua*, pages 55–63. Springer.

[56] Neuner, M. (2021). EdelweissFE. https://github.com/EdelweissFE/EdelweissFE.
[57] Neuner, M., Abrari Vajari, S., Arunachala, P. K., and Linder, C. (2023). A better understanding of the mechanics of borehole breakout utilizing a finite strain gradient-enhanced micropolar continuum model. *Computers and Geotechnics*, 153:105064.
[58] Neuner, M., Gamnitzer, P., and Hofstetter, G. (2020). A 3D gradient-enhanced micropolar damage-plasticity approach for modeling quasi-brittle failure of cohesive-frictional materials. *Computers & Structures*, 239:106332.
[59] Neuner, M., Hofer, P., and Hofstetter, G. (2022a). On the prediction of complex shear dominated concrete failure by means of classical and higher order damage-plasticity continuum models. *Engineering Structures*, 251:113506.
[60] Neuner, M., Regueiro, R. A., and Linder, C. (2022b). A unified finite strain gradient-enhanced micropolar continuum approach for modeling quasi-brittle failure of cohesive-frictional materials. *International Journal of Solids and Structures*, 254–255:111841.
[61] O'Hare, T. J., Gourgiotis, P. A., Coombs, W. M., and Augarde, C. E. (2024). An implicit Material Point Method for micropolar solids undergoing large deformations. *Computer Methods in Applied Mechanics and Engineering*, 419:116668.
[62] Oñate, E., Idelsohn, S. R., Del Pin, F., and Aubry, R. (2004). The particle finite element method — an overview. *International Journal of Computational Methods*, 1(02):267–307.
[63] Ord, A., Vardoulakis, I., and Kajewski, R. (1991). Shear band formation in Gosford Sandstone. *International Journal of Rock Mechanics and Mining Sciences & Geomechanics Abstracts*, 28(5):397–409.
[64] Peerlings, R. H. J., de Borst, R., Brekelmans, W. a. M., and Vree, J. H. P. D. (1996). Gradient Enhanced Damage for Quasi-Brittle Materials. *International Journal for Numerical Methods in Engineering*, 39(19):3391–3403.
[65] Pijaudier-Cabot, G. and Bažant, Z. P. (1987). Nonlocal damage theory. *Journal of Engineering Mechanics*, 113(10):1512–1533.
[66] Povolny, S. J., Seidel, G. D., and Tallon, C. (2021). Investigating the mechanical behavior of multiscale porous ultra-high temperature ceramics using a quasi-static material point method. *Mechanics of Materials*, 160:103976.
[67] Povolny, S. J., Seidel, G. D., and Tallon, C. (2022). Numerical Brazilian disk testing of multiscale porous Ultra-High Temperature Ceramics. *International Journal of Solids and Structures*, 234–235:111262.
[68] Poya, R., Gil, A. J., and Ortigosa, R. (2017). A high performance data parallel tensor contraction framework: Application to coupled electro-mechanics. *Computer Physics Communications*.
[69] Rogula, D. (1982). Introduction to Nonlocal Theory of Material Media. In Rogula, D., editor, *Nonlocal Theory of Material Media*, International Centre for Mechanical Sciences, pages 123–222. Springer, Vienna.
[70] Sadeghirad, A., Brannon, R., and Guilkey, J. (2013). Second-order convected particle domain interpolation (CPDI2) with enrichment for weak discontinuities at material interfaces. *International Journal for Numerical Methods in Engineering*, 95(11):928–952.
[71] Sadeghirad, A., Brannon, R. M., and Burghardt, J. (2011). A convected particle domain interpolation technique to extend applicability of the material point method for problems involving massive deformations. *International Journal for Numerical Methods in Engineering*, 86(12):1435–1456.
[72] Sołowski, W. T., Berzins, M., Coombs, W. M., Guilkey, J. E., Möller, M., Tran, Q. A., Adibaskoro, T., Seyedan, S., Tielen, R., and Soga, K. (2021). Material point method: Overview and challenges ahead. In *Advances in Applied Mechanics*, volume 54, pages 113–204. Elsevier.
[73] Sołowski, W. T. and Sloan, S. W. (2015). Evaluation of material point method for use in geotechnics. *International Journal for Numerical and Analytical Methods in Geomechanics*, 39(7):685–701.
[74] Steffen, M., Kirby, R. M., and Berzins, M. (2008a). Analysis and reduction of quadrature errors in the material point method (MPM). *International Journal for Numerical Methods in Engineering*, 76(6):922–948.
[75] Steffen, M., Wallstedt, P. C., Guilkey, J. E., Kirby, R. M., and Berzins, M. (2008b). Examination and Analysis of Implementation Choices within the Material Point Method (MPM). *Computer Modeling in Engineering & Sciences*, 31(2):107–128.
[76] Sulem, J. and Vardoulakis, I. (1990). Bifurcation analysis of the triaxial test on rock specimens. A theoretical model for shape and size effect. *Acta Mechanica*, 83(3-4):195–212.
[77] Sulsky, D., Chen, Z., and Schreyer, H. L. (1994). A particle method for history-dependent materials. *Computer Methods in Applied Mechanics and Engineering*, 118(1):179–196.
[78] Sulsky, D., Zhou, S.-J., and Schreyer, H. L. (1995). Application of a particle-in-cell method to solid mechanics. *Computer Physics Communications*, 87(1):236–252.
[79] Toupin, R. A. (1962). Elastic materials with couple-stresses. *Archive for Rational Mechanics and Analysis*, 11:385–414.
[80] Tran, Q.-A. and Sołowski, W. (2019). Generalized Interpolation Material Point Method modelling of large deformation problems including strain-rate effects – Application to penetration and progressive failure problems. *Computers and Geotechnics*, 106:249–265.
[81] Wallstedt, P. C. and Guilkey, J. E. (2008). An evaluation of explicit time integration schemes for use with the generalized interpolation material point method. *Journal of Computational Physics*, 227(22):9628–9642.
[82] Wang, B., Vardon, P. J., Hicks, M. A., and Chen, Z. (2016). Development of an implicit material point method for geotechnical applications. *Computers and Geotechnics*, 71:159–167.

[83] Wang, L., Coombs, W. M., Augarde, C. E., Cortis, M., Charlton, T. J., Brown, M. J., Knappett, J., Brennan, A., Davidson, C., Richards, D., and Blake, A. (2019). On the use of domain-based material point methods for problems involving large distortion. *Computer Methods in Applied Mechanics and Engineering*, 355:1003–1025.

[84] Wilson, P., Wüchner, R., and Fernando, D. (2021). Distillation of the material point method cell crossing error leading to a novel quadrature-based C0 remedy. *International Journal for Numerical Methods in Engineering*, 122(6):1513–1537.

[85] Yamaguchi, Y., Moriguchi, S., and Terada, K. (2021). Extended B-spline-based implicit material point method. *International Journal for Numerical Methods in Engineering*, 122(7):1746–1769.

[86] Zhang, D. Z., Ma, X., and Giguere, P. T. (2011). Material point method enhanced by modified gradient of shape function. *Journal of Computational Physics*, 230(16):6379–6398.

[87] Zhu, C., Wu, W., Peng, C., Wang, S., and Wei, X. (2024). SPH implementation of a critical state-based hypoplastic model for granular materials in large-deformation problems. *Computers and Geotechnics*, 166:106011.